Modeling Inelastic Behaviour Of Orthotropic Metals In A Unique Alignment Of Deviatoric Plane Within The Stress Space

Article *in* International Journal of Non-Linear Mechanics · December 2016

DOI: 10.1016/j.ijnonlinmec.2016.09.011

1 author:

Mohd Khir Mohd Nor
Universiti Tun Hussein Onn Malaysia
14 PUBLICATIONS **4** CITATIONS

International Journal of Non--Linear Mechanics 87 (2016) 43–57

Contents lists available at ScienceDirect

International Journal of Non–Linear Mechanics

journal homepage: www.elsevier.com/locate/nlm

Modelling inelastic behaviour of orthotropic metals in a unique alignment of deviatoric plane within the stress space

M.K. Mohd Nor[a,b,*]

[a] Crashworthiness and Collisions Research Group, Malaysia
[b] Universiti Tun Hussein Onn Malaysia, Beg Berkunci 101 Parit Raja, Batu Pahat, 86400 Johor, Malaysia

ARTICLE INFO

Keywords:
Constitutive formulation
Elastoplasticity
Orthotropic materials
Finite strain deformation

ABSTRACT

A finite strain constitutive model to predict the deformation behaviour of orthotropic metals is developed in this paper. The important features of this constitutive model are the multiplicative decomposition of the deformation gradient and a new Mandel stress tensor combined with the new stress tensor decomposition generalized into deviatoric and spherical parts. The elastic free energy function and the yield function are defined within an invariant theory by means of the structural tensors. The Hill's yield criterion is adopted to characterize plastic orthotropy, and the thermally micromechanical-based model, Mechanical Threshold Model (MTS) is used as a referential curve to control the yield surface expansion using an isotropic plastic hardening assumption. The model complexity is further extended by coupling the formulation with the shock equation of state (EOS). The proposed formulation is integrated in the isoclinic configuration and allows for a unique treatment for elastic and plastic anisotropy. The effects of elastic anisotropy are taken into account through the stress tensor decomposition and plastic anisotropy through yield surface defined in the generalized deviatoric plane perpendicular to the generalized pressure. The proposed formulation of this work is implemented into the Lawrence Livermore National Laboratory-DYNA3D code by the modification of several subroutines in the code. The capability of the new constitutive model to capture strain rate and temperature sensitivity is then validated. The final part of this process is a comparison of the results generated by the proposed constitutive model against the available experimental data from both the Plate Impact test and Taylor Cylinder Impact test. A good agreement between experimental and simulation is obtained in each test.

1. Introduction

In practice, in the real world, most of engineering materials such as composites and sheet metal components, manufactured using sheet metal forming processes, are orthotropic. Sheet forms of aluminium alloy are examples of orthotropic materials. Furthermore, many engineering materials such as fibre-reinforced elastomers or glassy polymers exhibit orthotropic behaviour while undergoing large elasto-plastic deformation, which can be observed at the unit-cell level due to the preferred orientations as a result of various manufacturing processes. At quasi-static rates of strain, this behaviour has been studied extensively by [72,66] while significant contributions to investigate the behaviour of metals that impacted with dynamic shock loading are due to [49,40,25,51,38,77,43,16]. Many have studied the influence of anisotropy on material behaviour undergoing finite strain deformation, including shock wave propagation, see for example [27,41–43,52,55,67,68,72].

A primary investigation of the shock response of aluminium alloys was made by [60] who showed in differently heat treated states, the Hugoniot Elastic Limit (HEL) and spall strengths for AA2024 followed the identical trends as the quasi-statically measured properties. Rosenberg showed that under both testing regimes, solution treated specimens possess the lowest strengths. Work by [47,48,12] on BCC tantalum, through a number of Taylor impact tests, predicted that evolution of texture does not affect the plastic deformation observed at continuum level. For a range of strain rates, it is shown that yield surface remained the same shape. This is the hypothesis used to support the assumption of isotropic hardening in this work.

A homogeneous yield function of degree two which is used to model an orthotropic plastic response of rolled sheet was first proposed by [29]. This concept can be regarded as a solid foundation for the subject in the case of metals. In the literature, numerous researchers have tried to investigate and examine the validity of this basic framework. The consensus is that the proposed model is too flexible and only well-

* Correspondance address: Department of Engineering Mechanics, Faculty of Mechanical and Manufacturing Engineering, Universiti Tun Hussein Onn Malaysia, Beg Berkunci 101 Parit Raja, Batu Pahat, 86400 Johor, Malaysia.
E-mail address: khir@uthm.edu.my.

http://dx.doi.org/10.1016/j.ijnonlinmec.2016.09.011
Received 16 February 2016; Received in revised form 23 September 2016; Accepted 23 September 2016
Available online 25 September 2016

suited to certain metals, as summarised by [34]. In addition to Hill's yield function, various types of yield functions have been presented in the literature. For the sake of brevity, only a few of them are briefly highlighted and grouped in this section, and a general comment is made accordingly.

The yield criteria modelled for metals can be found in [6,31,32,14,4] and others. The yield functions proposed in [6,31] are modelled for metals that are subjected to plane stress condition. The yield criteria proposed particularly for aluminium alloy sheets can be found in [7,9,39,13]. Further, Barlat and his group have proposed yield functions of the mth order in [6,7,9]. Constitutive models that are consistent with a micromechanical crystallographic-based yield criteria can be observed in [6,7]. In addition, a linear transformation-based anisotropic yield function can be found in [8,57,58] and others. Several non-quadratic yield criteria have been proposed by [26,30,44] and others.

For several reasons, not all of the above yield criteria are appropriately applicable to anisotropic materials. For example, some of the yield criteria are specified for isotropic materials and planar isotropy, which cannot be used to describe the behaviour of anisotropic materials. In addition, even though the yield criteria proposed by [30,44] are modelled for planar anisotropy, they have no shear components. Hence these models are not compatible in the case where the loadings are not co-linear with the anisotropic axes.

In addition, a few researchers such as Feigenbaum et al. have concentrated on distortional hardening as a consequence of internal variables' evolution, [17,22,23]. To track the results provided for these models, we refer to [22]. Generally this approach results in complexity of the model since more constants are introduced to describe the distortional hardening. However, the model as a whole has shown a capability to capture distortion of the yield surface for different loading paths and metals. On the other hand, most of the micromechanical based yield criteria can provide the required results. However they are not simple enough for fast numerical applications [15].

Some of the above yield criteria have been successfully implemented into finite element FE codes in order to model sheet metal forming processes as discussed in [15,70,35,76] and others. For instance, [15] have investigated Barlat's six components anisotropic yield function as proposed in [7] by modelling hydraulic bulge and cup drawing tests in ABAQUS. The same yield criterion has also been examined in [35] to investigate earing phenomena in the deep drawing of rolled aluminium sheets. Good agreements are obtained with respect to the experimental data. Earing can be observed developing in the early deformation phases and are influenced primarily by the initial texture of the tested aluminium sheets. In addition, the simulation showed that the evolution of texture has no effect upon the initial profiles of earing.

The yield criteria modelled in [6,29] are examined by [76] by simulating a stretch flange forming operation. The results obtained in the chosen numerical simulations show good agreement. This proves that these yield criteria are capable of simulating the forming processes. However, there are still theoretical problems: specifically the issues related to the rotation and distortion of the initial anisotropic reference frame [70]. A rigorous review and comments on the yield criteria proposed to capture the anisotropy of sheet metals can be found in [4].

The constitutive models intended to represent dynamic plastic behaviour are of great importance in the current design and analysis of forming processes due to various engineering applications, [13]. As discussed above, much research has been carried in this field, leading to results in various technologies involving analytical, experimental and computational methods. Despite of this current status, it is generally agreed that there is still a need for improved constitutive models as well as corresponding procedures to identify the parameters for these models. Moreover, the characterization of plastic deformation for orthotropic materials is still an open and exciting area of study even though there are many computer codes available for numerical analyses of intense impulsive loading due to high-velocity impact.

The theory related to isotropic materials is not very complex, as it may undergo rotations without affecting the material response. However, this is not the case for anisotropic materials. The mechanical properties that affect the yield surface will start to change (be distorted) when a material undergoing plastic deformation starts to rotate. Therefore, a set of variables has to be introduced to take into account the evolution and orientation of such materials. Generally speaking, anisotropic materials exhibit different mechanical properties in different directions which can be specified by magnitude and orientation. Even though there has been significant progress in computational methods and theoretical parts, there are still many issues relating to mechanical characteristics which have to be addressed. Moreover, there are numerous mechanics of materials issues that have yet to be solved, related to orthotropic elastic and plastic behaviour. The prime motivation in this work, therefore, is to propose a new constitutive model that is capable for modelling of the deformation behaviour of such materials undergoing finite strain deformation.

2. New stress tensor decomposition

The shock response of an orthotropic material cannot be accurately predicted using the conventional decomposition of the stress tensor into isotropic and deviatoric parts, [1]. Constitutive models developed for the modelling of shock wave propagation in solids comprise of two parts, an equation of state (EOS) and a strength model which define the response of the material to uniform compression (change of volume) and the response of the material to shear deformation (change of shape), respectively. This separation of material response into volumetric and deviatoric strain components is matched for isotropic materials which have an isotropic elastic stiffness tensor c_{ijkl}. As a consequence the spherical part of the stress tensor $-P\delta_{ij}=c_{ijkl}\delta_{kl}\varepsilon_{pp}/3$, being a product of two isotropic tensors, is itself isotropic. Furthermore, the isotropy of c_{ijkl} results in the co-linearity of the principal axes of the stress and strain tensors. In other words, components of stress and strain are proportional to each other and orthogonality between the volumetric and deviatoric components of strain is reflected in orthogonality between the volumetric and deviatoric components of stress. This is successfully done for isotropic materials through the conventional decomposition of the stress tensor into the spherical and deviatoric parts.

However, in the case of orthotropic materials this co-linearity is not in place. Hence the equivalent relationship cannot be defined for orthotropic materials. If one maintains the assumption that pressure is the state of stress induced by an isotropic state of strain (uniform compression or expansion) then a more general definition of pressure is required, [73]. This leads to a number of possible definitions of pressure as a vector in the principal stress space which is not co-linear with the conventional hydrostatic alignment for orthotropic materials. To explore this statement further Vignjevic has proposed a new expression for generalized pressure or stress related to uniform compression. The ability to describe shock propagation in orthotropic materials is investigated with experimental plate impact data and showed a good agreement with the physical behaviour of the considered material (carbon fibre reinforced epoxy).

To derive the formulation of this generalized pressure, let us first write the stress due to the isotropic component of strain (isotropic strain pressure) as

$$-\widetilde{P}\psi_{ij}=c_{ijkl}\delta_{kl}\varepsilon_{ss}/3=c_{ijkk}\varepsilon_v \tag{1}$$

where $\psi_{ij}=0\ \forall\ i\neq j$, $\psi_{ij}\neq 0\ \forall\ i=j$, and $\varepsilon_v=\varepsilon_{ss}/3$. In above equation, $\widetilde{P}$ and ψ_{ij} can be defined as

$$-\widetilde{P}=\varepsilon_v\sqrt{\frac{1}{\psi_{st}\psi_{st}}c_{ijkk}c_{ijll}} \tag{2}$$

and

$$\psi_{ij}=-c_{ijkk}\varepsilon_v/\tilde{P}=c_{ijkk}/\sqrt{\frac{1}{\psi_{st}\psi_{st}}c_{prkk}c_{prll}} \tag{3}$$

The double contraction tensor $\psi_{st}\psi_{st}$ must be defined to uniquely define $\tilde{P}$ and tensor ψ_{ij}. One possible assumption is to set $\psi_{st}\psi_{st}=3$. Note that the tensor ψ_{ij} is fully defined by the material elastic stiffness properties. Further, Eqs. (1)–(3) can be expressed in Voigt notation as shown in Eqs. (4)–(6) respectively:

$$\tilde{P}\begin{Bmatrix}\psi_1\\ \psi_2\\ \psi_3\\ 0\\ 0\\ 0\end{Bmatrix}=-\begin{bmatrix}c_{11} & c_{12} & c_{13} & 0 & 0 & 0\\ c_{12} & c_{22} & c_{23} & 0 & 0 & 0\\ c_{13} & c_{23} & c_{33} & 0 & 0 & 0\\ 0 & 0 & 0 & c_{44} & 0 & 0\\ 0 & 0 & 0 & 0 & c_{55} & 0\\ 0 & 0 & 0 & 0 & 0 & c_{66}\end{bmatrix}\begin{Bmatrix}\varepsilon_v\\ \varepsilon_v\\ \varepsilon_v\\ 0\\ 0\\ 0\end{Bmatrix} \tag{4}$$

The scalar $\tilde{P}$ which is used to define the magnitude of pressure can be expressed as

$$\tilde{P}=-\sqrt{\frac{(c_{11}+c_{12}+c_{13})^2+(c_{12}+c_{22}+c_{23})^2+(c_{13}+c_{23}+c_{33})^2}{3}}\varepsilon_v=-3K_\psi\varepsilon_v \tag{5}$$

The parameter K_ψ reduces to the conventional bulk modulus in the limit of material isotropy. ψ_{ij} which is used defines the direction of the new volumetric axis in stress space then can be defined as

$$\psi_{(ii)}=\frac{c_{i1}+c_{i2}+c_{i3}}{\sqrt{\frac{(c_{11}+c_{12}+c_{13})^2+(c_{12}+c_{22}+c_{23})^2+(c_{13}+c_{23}+c_{33})^2}{3}}} \tag{6}$$

Repeated indices in brackets in the above equation indicate no summation. The alternative formulation of generalized pressure for orthotropic materials can finally be expressed as follows:

$$\tilde{P}=\frac{\sigma_{kl}\psi_{kl}}{\psi_{sr}\psi_{sr}} \tag{7}$$

It should be noted that ψ_{ij} becomes δ_{ij} when dealing with isotropic materials. Hence the new decomposition reduces to the conventional decomposition developed for isotropic materials. This new stress tensor decomposition has been used to develop a new yield criterion for orthotropic sheet metals under plane-stress conditions by assuming the yield surface to be circular in the new deviatoric plane [53]. The predictions of the new effective stress expression showed good agreement with respect to the experimental data for 6000 series aluminium alloy sheet (A6XXX-T4) and Al-killed cold-rolled steel sheet SPCE [5].

2.1. Representation in stress space

The representation of the new stress tensor decomposition in stress space is presented in this section. Bear in mind that any arbitrary stress state in stress space can be decomposed into hydrostatic and deviatoric parts. This representation which is applied for isotropic materials as shown in Eq. (7) is best presented in 3- and 2-dimensional stress spaces by red lines in Figs. 1 and 2 with their directions perpendicular to each other. Recalling the new stress tensor decomposition, the representations of this decomposition ψ_{ij} in 3- and 2-dimensional stress spaces are shown in Figs. 1 and 2 by green lines respectively. These figures represent the graphical interpretation of the generalized pressure axes of the new decomposition ψ_{ij} in 3- and 2-dimensional stress spaces respectively. From these figures, it can be observed that this decomposition leads to a shift of the pressure vector away from the common alignment (equal angle with the principal stress directions). Equally, it can be observed that the direction of the volumetric axis ψ_{ij} is not making the same angle with the principal stress directions. Based on the definition of the new stress tensor decomposition, any considered orthotropic materials will uniquely define their own deviatoric plane within the stress space.

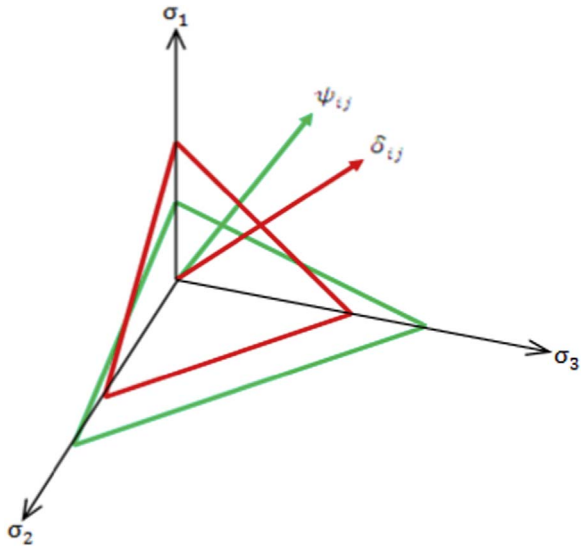

Fig. 1. ψ and δ as a vectors in a principal stress space. (For interpretation of the references to colour in this figure, the reader is referred to the web version of this article.)

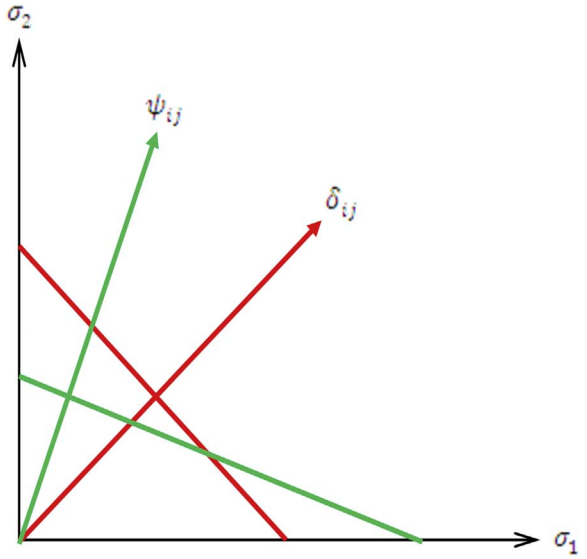

Fig. 2. ψ and δ representation in 2-dimensional stress space. (For interpretation of the references to colour in this figure, the reader is referred to the web version of this article.)

3. New constitutive model formulation

3.1. Kinematics for finite strain deformations

The construction of the new hyperelastic-plastic constitutive model for orthotropic metals in this paper is based on the multiplicative decomposition of the deformation gradient **F**:

$$\mathbf{F}=\mathbf{F}_e\mathbf{F}_p \tag{8}$$

where F_e and F_p represent thermo-elastic part of the deformation and plastic part of the deformation (dislocation mechanics), respectively. This concept distinguishes the proposed constitutive model from hypoelastic-plastic material models (when elastic strains are small compared to the plastic strains). The intermediate (generally non-Euclidean) configuration corresponds to elastically unloaded material, known as the elastic reference configuration which can be physically obtained by elastic unloading of material (unstressed condition). The formulation based on additive decomposition of generalized strain measures is avoided in this work. As demonstrated by [36], this formulation leads to spurious shear stresses which are independent

of the elastic material properties for orthotropic materials. In addition, the evolution of material symmetry in orthotropic materials due to large deformations could not be tracked by the additive strain decomposition based model [37].

Using Eq. (8), the elastic right Cauchy-Green tensor $\mathbf{C}_e$ and the elastic Green-Lagrange strain tensor $\mathbf{E}_e$ are

$$\mathbf{C}_e=\mathbf{F}_e^T\bullet\mathbf{F}_e,\quad \mathbf{E}_e=\frac{1}{2}(\mathbf{C}_e-\mathbf{I})=\frac{1}{2}(\mathbf{F}_e^T\bullet\mathbf{F}_e-\mathbf{I}) \tag{9}$$

The experimental work in [45] shows a strong correlation between elastic and plastic material symmetries. Therefore, the constitutive model described in this paper is developed and integrated in the isoclinic configuration. In other words, the hyperelastic part of the constitutive model is based on the assumption that the principal directions of material elastic and plastic orthotropy coincide and are not influenced by inelastic deformation. The requirements that free strain energy function is invariant under transformations of material symmetry and the non-uniqueness of the intermediate configuration are directly resolved by working in this configuration. This definition gives a significant simplification to the numerical implementation of the corresponding constitutive equations because one can steer clear of the explicit use of any corotational rate, [2]. To avoid confusion, (∧) is used in this paper upon each of kinematic and kinetic variables defined with respect to the isoclinic configuration.

The structural tensors $\mathbf{M}_{ii}|i=1,2,3$ [11] are introduced to construct the orthotropy symmetric group ϑ. These tensors can be defined as $\mathbf{M}_1=\mathbf{n}_1\otimes\mathbf{n}_1$, $\mathbf{M}_2=\mathbf{n}_2\otimes\mathbf{n}_2$ and $\mathbf{M}_3=\mathbf{n}_3\otimes\mathbf{n}_3$ where $\mathbf{n}_1$, $\mathbf{n}_2$ and $\mathbf{n}_3$ are unit vectors represent an orthonormal frame of the material. By using the structural tensors $\hat{\mathbf{M}}_{ii}|i=1,2,3$ in the isoclinic configuration, the elastic free strain energy function for orthotropic materials considers the principal directions of material elastic orthotropy (material symmetry) in this configuration to be aligned with the unit (director) vectors $\hat{\mathbf{n}}_1$, $\hat{\mathbf{n}}_2$ and $\hat{\mathbf{n}}_3$. As shown in Fig. 3, push forward transformations of the structural tensors from an initial configuration $\boldsymbol{\Omega}_o$ to elastically unloaded configuration $\overline{\boldsymbol{\Omega}}_p$ can be defined as $\mathbf{M}_{ii}=\mathbf{F}_p\mathbf{M}_{ii}\mathbf{F}_p^{-1}$. The structural tensors $\mathbf{M}_{ii}$ are pulled back from the elastically unloaded configuration (having an arbitrary orientation) $\overline{\boldsymbol{\Omega}}_p$ to the isoclinic configuration $\hat{\boldsymbol{\Omega}}_i$ by rotating back for plastically induced rigid body rotation due to plastic related deformations using below orthonormal transformation.

$$\hat{\mathbf{M}}_{ii}=\mathbf{Q}_p^T\mathbf{M}_{ii}\mathbf{Q}_p \tag{10}$$

where $\mathbf{Q}_p$ is an orthonormal tensor that defines the rigid rotation due to plastic related deformation.

Referring to Fig. 3, a triad of unit vectors which represent the material symmetries is schematically shown by two orthogonal axes with arrows. Both elastic stretching and rotation are contained in the elastic part $\mathbf{F}_e$ of the deformation gradient $\mathbf{F}$. Plastic part of $\mathbf{F}$ with respect to $\overline{\boldsymbol{\Omega}}_p$ and $\hat{\boldsymbol{\Omega}}_i$ is represented by $\mathbf{F}_p$ and $\hat{\mathbf{F}}_p$ respectively. The

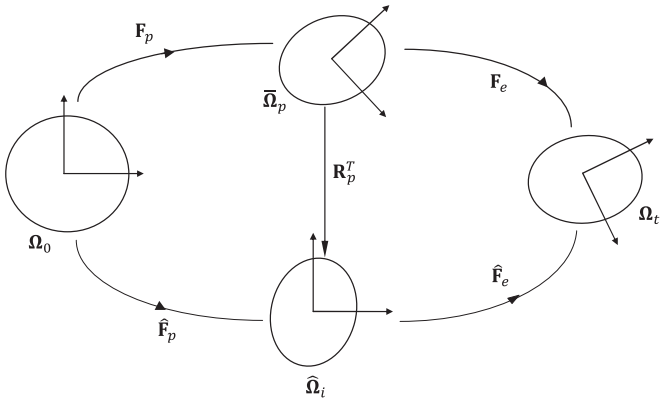

Fig. 3. Definition of isoclinic configuration.

plastic rotation $\mathbf{R}_p$ is assigned to $\mathbf{F}_p$ to ensure there is no rotation to the material principal axes of orthotropy (remains fixed or unaltered by plastic deformation) in the isoclinic configuration $\hat{\boldsymbol{\Omega}}_i$.

As examined in [64], the rotation and distortion during elastoplastic deformation are contained in the elastic part of $\mathbf{F}$ as a result of isoclinic configuration. Despite of general incompatibility tensor fields between elastic and plastic deformations, the elastic deformation may incidentally be compatible with plastic deformation when plastic or elastic deformation is homogeneous [64]. Alternatively, the plastic rotation $\mathbf{R}_p$ can be assigned to the deformation due to damage $\mathbf{F}_d$ to define $\hat{\mathbf{F}}_e=\mathbf{F}_e\mathbf{F}_d\mathbf{R}_p$ if one considers the elastic material parameters to evolve due to damage since the changes of material compliance due to damage [71]. This assumption however not considered in this work.

The elastic and plastic parts of the deformation gradient $\mathbf{F}$ of the proposed constitutive formulation then can be defined explicitly in the isoclinic configuration as:

$$\hat{\mathbf{F}}_e=\mathbf{F}_e,\quad \hat{\mathbf{F}}_p=\mathbf{R}_p^T\mathbf{F}_p=\mathbf{R}_p^T\mathbf{R}_p\mathbf{U}_p=\mathbf{U}_p \tag{11}$$

where plastic rotation $\mathbf{R}_p$ is an orthogonal rotation tensor induced by plastic deformation and $\mathbf{U}_p$ refers to plastic right stretch tensor. Subsequently, the total velocity gradient $\hat{\mathbf{L}}$ can be decomposed additively into elastic $\hat{\mathbf{L}}_e$ and plastic $\hat{\mathbf{L}}_p$ parts. The incompressibility constraint is assumed to hold for plastic deformation which therefore gives

$$\det(\hat{\mathbf{F}}_p)=1 \tag{12}$$

3.2. Mandel stress tensor

In general, the Mandel stress tensor $\boldsymbol{\Sigma}$ can be defined as follows [46]:

$$\boldsymbol{\Sigma}=\mathbf{C}\bullet\boldsymbol{S} \tag{13}$$

where $\mathbf{C}$ and $\boldsymbol{S}$ refer to Right Cauchy-Green tensor and Second Piola Kirchhoff stress tensor respectively. These tensors can be expressed in the elastically unloaded intermediate configuration $\overline{\boldsymbol{\Omega}}_p$ as

$$\overline{\mathbf{C}}_e=\mathbf{F}_e^T\bullet\mathbf{F}_e \tag{14}$$

$$\overline{\boldsymbol{S}}=\mathbf{F}_e^{-1}\bullet\boldsymbol{\tau}\bullet\mathbf{F}_e^{-T} \tag{15}$$

The Kirchhoff stress tensor $\boldsymbol{\tau}$ in Eq. (15) is a symmetric tensor defined in the current configuration $\boldsymbol{\Omega}_t$ as

$$\boldsymbol{\tau}=\boldsymbol{J}\bullet\boldsymbol{\sigma}=\det(\mathbf{F})\bullet\boldsymbol{\sigma} \tag{16}$$

where J is a volume ratio. Substituting Eqs. (14) and (15) into Eq. (13), the Mandel stress tensor in the intermediate configuration $\overline{\boldsymbol{\Omega}}_p$ can be defined as

$$\overline{\boldsymbol{\Sigma}}=\mathbf{F}_e^T\bullet\boldsymbol{\tau}\bullet\mathbf{F}_e^{-T}=\det(\mathbf{F})\bullet\mathbf{F}_e^T\bullet\boldsymbol{\sigma}\bullet\mathbf{F}_e^{-T} \tag{17}$$

The Mandel stress tensor defined in Eq. (17) is frequently used to describe the behaviour of plastic materials [33]. This stress tensor is adopted in this work to formulate the new constitutive model for orthotropic metals. Choosing the isoclinic configuration $\hat{\boldsymbol{\Omega}}_i$ as a point for integration, the Mandel stress tensor can be rewritten as

$$\hat{\boldsymbol{\Sigma}}=\hat{\mathbf{F}}_e^T\bullet\boldsymbol{\tau}\bullet\hat{\mathbf{F}}_e^{-T} \tag{18}$$

Further, Eq. (17) also can be expressed as follows:

$$\hat{\boldsymbol{\Sigma}}=\hat{\mathbf{F}}_e^T\bullet\boldsymbol{\tau}\bullet\hat{\mathbf{F}}_e^{-T}=\hat{\mathbf{F}}_e^T\bullet\det(\mathbf{F})\bullet\boldsymbol{\sigma}\bullet\hat{\mathbf{F}}_e^{-T}=\det(\mathbf{F})\bullet\hat{\mathbf{F}}_e^T\bullet\boldsymbol{\sigma}\bullet\hat{\mathbf{F}}_e^{-T} \tag{19}$$

Using $\sigma_{ij}=P\delta_{ij}+S_{ij}$, the above equation can be defined as

$$\hat{\boldsymbol{\Sigma}}=\det(\mathbf{F})\bullet\hat{\mathbf{F}}_e^T\bullet\boldsymbol{\sigma}\bullet\hat{\mathbf{F}}_e^{-T}=\det(\mathbf{F})\bullet\hat{\mathbf{F}}_e^T\bullet(P\boldsymbol{\delta}+\mathbf{S})\bullet\hat{\mathbf{F}}_e^{-T} \tag{20}$$

The formulation of the new generalized pressure for orthotropic metals is introduced in Eq. (20):

$$\hat{\boldsymbol{\Sigma}}=\det(\mathbf{F})\bullet\hat{\mathbf{F}}_e^{T}\bullet\left(\mathbf{S}+\frac{\sigma\boldsymbol{\psi}}{\boldsymbol{\psi}\boldsymbol{\psi}}\bullet\boldsymbol{\psi}\right)\bullet\hat{\mathbf{F}}_e^{-T} \tag{21}$$

Eq. (21) can be further extended as

$$\hat{\boldsymbol{\Sigma}}=\underbrace{\det(\mathbf{F})\bullet\hat{\mathbf{F}}_e^{T}\bullet\mathbf{S}\bullet\hat{\mathbf{F}}_e^{-T}}_{\hat{\boldsymbol{\Sigma}}'=\text{deviatoric}}+\underbrace{\det(\mathbf{F})\bullet\hat{\mathbf{F}}_e^{T}\bullet\frac{\sigma\boldsymbol{\psi}}{\boldsymbol{\psi}\boldsymbol{\psi}}\bullet\boldsymbol{\psi}\bullet\hat{\mathbf{F}}_e^{-T}}_{\hat{\boldsymbol{\Sigma}}_p} \tag{22}$$

where $\hat{\boldsymbol{\Sigma}}_p$ denotes the volumetric part (pressure) of the new Mandel stress tensor. Focusing on the deviatoric part instead of a full stress tensor, the deviatoric part of the new Mandel stress tensor is given by

$$\hat{\boldsymbol{\Sigma}}'=\det(\mathbf{F})\bullet\hat{\mathbf{F}}_e^{T}\left(\boldsymbol{\sigma}-\frac{\sigma\boldsymbol{\psi}}{\boldsymbol{\psi}\boldsymbol{\psi}}\bullet\boldsymbol{\psi}\right)\hat{\mathbf{F}}_e^{-T} \tag{23}$$

Finally the new deviatoric Mandel stress tensor defined in the isoclinic configuration $\overline{\boldsymbol{\Omega}}_i$, can be written as

$$\hat{\boldsymbol{\Sigma}}'=\underbrace{\det(\mathbf{F})\bullet\hat{\mathbf{F}}_e^{T}\bullet\boldsymbol{\sigma}\bullet\hat{\mathbf{F}}_e^{-T}}_{\hat{\boldsymbol{\Sigma}}}-\underbrace{\det(\mathbf{F})\bullet\hat{\mathbf{F}}_e^{T}\bullet\frac{\sigma\boldsymbol{\psi}}{\boldsymbol{\psi}\boldsymbol{\psi}}\bullet\boldsymbol{\psi}\bullet\hat{\mathbf{F}}_e^{-T}}_{\hat{\boldsymbol{\Sigma}}_p}=\det(\mathbf{F})\bullet\hat{\mathbf{F}}_e^{T}\bullet\mathbf{S}\bullet\hat{\mathbf{F}}_e^{-T} \tag{24}$$

It can be easily proven the deviatoric component of the new Mandel stress tensor Eq. (24) is traceless (deviator tensor). As asserted in [54], existing experimental evidence shows that it is hard to deduce sound data about a continuum elastic domain for the skew-symmetric part of the Mandel stress tensor $\boldsymbol{\Sigma}_a$. Much effort still required in terms of experimental work to establish the elastic domain and yield functions for the skew-symmetric part of the Mandel stress tensor. Therefore, in this work, only the symmetric part of the Mandel stress is considered [59,74].

A thermodynamics analysis presented in Section 3.6 is based on the second law in the form of Clausius–Plank (CP) inequality, defined in the isoclinic configuration $\hat{\boldsymbol{\Omega}}_i$. In order to define the CP inequality, it is necessary to introduce relevant conjugate variable pairs, starting with the stress power $\mathcal{P}$.

$$\mathcal{P}=\boldsymbol{\tau}:\mathbf{L}=\det(\mathbf{F})\bullet\boldsymbol{\sigma}:\mathbf{L}=\boldsymbol{S}:\dot{\mathbf{E}}=\hat{\boldsymbol{\Sigma}}':\hat{\mathbf{L}}_p \tag{25}$$

The stress power characterizes the real mechanical power during dynamic process. The representation of stress power is the product of work conjugate stress and strain measures. This thermodynamic part of the constitutive model is further discussed in Section 3.6.

3.3. Coupling of the proposed stress decomposition with equation of state EOS

In recent decades, the topic related to shock wave propagation in anisotropic materials has received considerable attention in the isotropic solid-state physics and mechanics literature [18,19,21,3,50,75,78]. Appropriate constitutive equations to describe the strength effect and the equation of state must be investigated to describe the anisotropic material response under shock loading. Therefore, in this work, the formulation is combined with an equation of state (EOS) in addition to the conservation laws to mathematically describe the material's nonlinear behaviour and propagation of strong shock waves in solids due to shock loading.

An EOS represents a closure equation, which completes the relationships between the state variables in front of and behind a shockwave. Theoretically, the relationship described by EOS can be determined from the thermodynamic properties of the material, and require no dynamic data. However, practically, extensive dynamic experiments such as the planar shock wave experiment are required to characterize data on the material's behaviour at high strain rates. In contemporary hydrocodes EOS's are either of an analytical or a tabulated type. In this paper a very popular EOS that is extensively used for solid continua, the Mie-Gruneisen EOS [69,28], implemented in DYNA3D, is used. This an analytic EOS frequently used with solid materials. It defines the pressure as a function of density ρ or specific volume and specific internal energy e as shown below

$$\boldsymbol{P}=\boldsymbol{f}(\boldsymbol{\rho},\ \boldsymbol{e})=\boldsymbol{p}_r(\mathrm{v})+\frac{(\mathrm{v})}{\mathrm{v}}(\boldsymbol{e}-\boldsymbol{e}_r(\mathrm{v})) \tag{26}$$

where v is the specific volume, (v) is the Grunesien gamma defined as

$$(\mathrm{v})=\mathrm{v}\left(\frac{\partial\boldsymbol{P}}{\partial\boldsymbol{e}}\right)_{\mathrm{v}} \tag{27}$$

Generally is defined as constant $=\ _0$, or assumed that $\frac{_0}{\mathrm{v}_0}=\frac{-}{\mathrm{v}}=\text{const}$ alternatively. The functions p_r and e_r are considered known functions of v on some reference curve. There are few possible reference curves to name such as the shock Hugoniot curve, the 0 °K isotherm, etc. However the most widely adopted form of the Mie-Gruneisen equation of state for solid materials which uses the shock Hugoniot as the reference curve is defined as follows

$$\boldsymbol{P}=\boldsymbol{f}(\boldsymbol{\rho},\ \boldsymbol{e})=\boldsymbol{p}_H\bullet+\left(1-\frac{}{2}\boldsymbol{\mu}\right)+\boldsymbol{\rho}\ \boldsymbol{e} \tag{28}$$

where p_H refers to Hugoniot pressure, $\mu=\frac{\rho}{\rho_0}-1$ is relative change of volume, is Gruneisen parameter, ρ is density and e is the specific internal energy. The Rankine–Hugoniot equations for the shock jump conditions can be regarded by defining a relation between any pair of the ρ, P, e, u_p (the velocity of the particle directly behind the shock) and U (the velocity of shockwave that propagates through the medium). There is an empirical linear relationship between U and u_p for many liquids and most solids:

$$\boldsymbol{U}=\boldsymbol{c}+\boldsymbol{S}\boldsymbol{u}_p \tag{29}$$

where c is the intercept of the $U-u_p$ curve (U-shock velocity vs. u_p particle velocity curve), and S is the coefficient of the $U-u_p$ curve slope. The Hugoniot pressure and a shock velocity normally U are normally defined as a non-linear function of particle velocity u_p as follows [69]:

$$\boldsymbol{U}=\boldsymbol{c}+\boldsymbol{S}_1\boldsymbol{u}_p+\boldsymbol{S}_2\left(\frac{\boldsymbol{u}_p}{\boldsymbol{U}}\right)\boldsymbol{u}_p+\boldsymbol{S}_3\left(\frac{\boldsymbol{u}_p}{\boldsymbol{U}}\right)^2\boldsymbol{u}_p \tag{30}$$

The Gruneisen's gamma for the undeformed materials can be expressed by

$$=\frac{\gamma_0+\boldsymbol{a}\boldsymbol{u}}{1+\boldsymbol{u}} \tag{31}$$

Hence, the pressure as a function of Gruneisen equation of state with cubic shock velocity can be defined as

$$\begin{aligned}P_{EOS}&=\frac{\rho_0c^2\mu\left[1+\left(1-\frac{\Gamma}{2}\right)\mu-\frac{\Gamma}{2}\mu^2\right]}{\left[1-(S_1-1)\mu-S_2\frac{\mu^2}{\mu+1}-S_3\frac{\mu^3}{(\mu+1)^2}\right]^2}+(1+\mu)\,\Gamma\,E \quad \text{when } \mu>0\\ P_{EOS}&=\rho_0c^2\mu+(1+\mu)\Gamma\,E \quad \text{when } \mu<0\end{aligned} \tag{32}$$

where
E is the internal energy per initial specific volume,
$S_1,\ S_2,\ S_3$ are the coefficients of the slope of the $U-u_p$ curve,
γ_0 is the Gruneisen gamma for the un-deformed material,
a is the first order volume correction to γ_0,
$c, S_1,\ S_2,\ S_3,\ \gamma_0, a, \rho_0$ represent the material properties supplied by the user to characterize this EOS.

The combination between the proposed stress tensor decomposition and the Mie-Gruneisen EOS requires some modifications to reflect the formulation of the generalized orthotropic pressure. Briefly, $\boldsymbol{\psi}$ is calculated using the material stiffness matrix $\boldsymbol{C}$ read from the input file. The increment of deviatoric Mandel stress tensor $\hat{\boldsymbol{\Sigma}}'$ is then calculated using rate of deformation tensor $\mathbf{D}$. By setting pressure equals to P_{EOS}, $\widetilde{P}=P_{EOS}$, the stress update at time $n+1$ can be defined as

$$\boldsymbol{\sigma}^{n+1}=\hat{\boldsymbol{\Sigma}}'^{n+1}-\boldsymbol{P}_{\boldsymbol{EOS}}^{\boldsymbol{n+1}}\boldsymbol{\psi} \tag{33}$$

3.4. Orthotropy of elastic free energy function

To model the behaviour of orthotropic metals within elastic and plastic regimes the formulation of orthotropic tensor functions is constructed as a free strain energy function and a plastic level set function (orthotropic yield criterion). These tensor functions are defined fundamentally based on the representation of isotropic tensor functions theory. As aforementioned, a material symmetry group ϑ is defined in this work to develop anisotropic tensor function for orthotropic constitutive behaviour. This orthotropic symmetric group is assumed to be unchanged during plastic deformation. Furthermore, the isotropic tensor function must be invariant under the special orthogonal group [20].

The elastic orthotropy of the proposed formulation is defined using the Helmholtz free energy as a function of evolving structural tensors. The Helmholtz free energy in the isoclinic configuration $\hat{\boldsymbol{\Omega}}_i$ is additively decomposed into elastic and plastic parts as

$$\hat{\boldsymbol{\Psi}}=\hat{\boldsymbol{\Psi}}_e(\hat{\mathbf{E}}_e)+\hat{\boldsymbol{\Psi}}_{p(isot)}(\boldsymbol{\alpha}) \tag{34}$$

In the above expression, $\hat{\Psi}_e(\hat{\mathbf{E}}_e)$ represents the energy stored due to elastic deformations defined in terms of Elastic Green-Lagrange strain tensor $\hat{\mathbf{E}}_e$. In addition, $\hat{\Psi}_{p(isot)}(\alpha)$ represents energy resulting from isotropic plastic hardening, where α is the isotropic hardening variable (i.e. accumulated plastic deformation). The response of elastic material in the isoclinic configuration must be invariant under transformations of the material symmetry group ϑ. This is necessary based on the definition of isotropic functions.

$$\hat{\boldsymbol{\Psi}}_e(\mathbf{Q}^T\hat{\mathbf{E}}_e\mathbf{Q})=\hat{\boldsymbol{\Psi}}_e(\hat{\mathbf{E}}_e),\forall\mathbf{Q}\in\boldsymbol{\vartheta},\ \hat{\mathbf{E}}_e \tag{35}$$

where $\mathbf{Q}$ is orthogonal rotation tensor. $\hat{\Psi}_e$ is then known as a ϑ-invariant function. Using the structural tensors $\hat{\mathbf{M}}_{ii}$, the elastic component of free energy function for orthotropic materials can be expressed in terms of isotropic function in the isoclinic configuration as follows:

$$\hat{\boldsymbol{\Psi}}_e=\hat{\boldsymbol{\Psi}}_e(\hat{\mathbf{E}}_e,\ \hat{\mathbf{M}}_{11},\ \hat{\mathbf{M}}_{22})=\hat{\boldsymbol{\Psi}}_e(\mathbf{Q}\hat{\mathbf{E}}_e\mathbf{Q}^T,\ \mathbf{Q}\hat{\mathbf{M}}_{11}\mathbf{Q}^T,\ \mathbf{Q}\hat{\mathbf{M}}_{22}\mathbf{Q}^T) \tag{36}$$

$\hat{\Psi}_e$ can be further defined in terms of a set of invariants of the Elastic Green-Lagrange strain tensor $\hat{\mathbf{E}}_e$ [20] such as

$$J_1=\mathbf{tr}\widehat{\mathbf{E}_e},\quad J_2=\mathbf{tr}[(\widehat{\mathbf{E}_e})^2],\quad J_3=\mathbf{tr}[(\widehat{\mathbf{E}_e})^3] \tag{37}$$

Using structural tensors that reflect the material symmetry of orthotropic materials, the irreducible invariants and the additional pseudo-invariants in the isoclinic configuration $\hat{\boldsymbol{\Omega}}_i$ can be expressed as follows [79,65,20] etc.

$$J_4=tr[\widehat{\mathbf{M}_{11}}\widehat{\mathbf{E}_e}],\quad J_5=tr[\widehat{\mathbf{M}_{11}}(\widehat{\mathbf{E}_e})^2],\quad J_6=tr[\widehat{\mathbf{M}_{22}}\widehat{\mathbf{E}_e}],\quad J_7=tr[\widehat{\mathbf{M}_{22}}(\widehat{\mathbf{E}_e})^2] \tag{38}$$

Subsequently, the elastic free energy function $\hat{\Psi}_e$ can be expressed in a quadratic form as

$$\hat{\Psi}_e=\frac{1}{2}\lambda J_1^2+\mu J_2+\frac{1}{2}o_1J_4^2+\frac{1}{2}o_2J_6^2+2o_3J_5+2o_4J_7+o_5J_4J_1+o_6J_6J_1+o_7J_4J_6 \tag{39}$$

where $\lambda,\ \mu,\ o_i|_{i=1,..7}$ in this case represent material parameters for the elastic orthotropic material. The second Piola-Kirchhoff stress tensor $\hat{\boldsymbol{S}}$ in the isoclinic configuration $\hat{\boldsymbol{\Omega}}_i$ can be derived as $\hat{\boldsymbol{S}}=\frac{\partial\hat{\Psi}_e}{\partial\hat{\mathbf{E}}_e}$, while the constant fourth-order tensor $\hat{\mathbb{M}}$ is obtained by the second derivative of $\hat{\Psi}_e$. Eventually the constant fourth-order tensor $\hat{\mathbb{M}}$ that consists of the structural tensors $\hat{\mathbf{M}}_{ii}|i=1,2,3$ can be defined in the isoclinic configuration $\hat{\boldsymbol{\Omega}}_i$ as

$$\begin{aligned}\hat{\mathbb{M}}=&\lambda\mathbf{I}\otimes\mathbf{I}+2\mu\mathbb{I}+o_1\hat{\mathbf{M}}_{11}\otimes\hat{\mathbf{M}}_{11}+o_2\hat{\mathbf{M}}_{22}\otimes\hat{\mathbf{M}}_{22}+2o_3\mathbb{K}_1+2o_4\\&\mathbb{K}_2+o_5(\hat{\mathbf{M}}_{11}\otimes\mathbf{I}+\mathbf{I}\otimes\hat{\mathbf{M}}_{11})+o_6(\hat{\mathbf{M}}_{22}\otimes\mathbf{I}+\mathbf{I}\otimes\hat{\mathbf{M}}_{22})+o_7\\&(\hat{\mathbf{M}}_{11}\otimes\hat{\mathbf{M}}_{22}+\hat{\mathbf{M}}_{22}\otimes\hat{\mathbf{M}}_{11})\end{aligned} \tag{40}$$

where

$$\mathbb{I}=\mathbb{I}_{ijkl}=\delta_{ik}\delta_{jl}\ \ (\text{fourth}-\text{order unit tensor})\mathbb{K}_1=\boldsymbol{\delta}_{ik}\hat{\mathbf{M}}^1_{jl}+\boldsymbol{\delta}_{jl}\hat{\mathbf{M}}^1_{ik},$$

$$\mathbb{K}_2=\boldsymbol{\delta}_{ik}\hat{\mathbf{M}}^2_{jl}+\boldsymbol{\delta}_{jl}\hat{\mathbf{M}}^2_{ik} \tag{41}$$

Note that the conventional relation between stress and strain tensor in the isoclinic configuration $\hat{\boldsymbol{\Omega}}_i$ can be expressed as follows:

$$\hat{\boldsymbol{S}}_{ij}=\hat{\mathfrak{c}}_{ijkl}\hat{\mathbf{E}}_{kl} \tag{42}$$

where $\mathfrak{c}_{ijkl}$ is a fourth-order elasticity or material stiffness tensor. This tensor can be set equal to $\hat{\mathbb{M}}$ to define $\lambda,\ \mu,\ o_i|_{i=1,..7}$ with respect to the elasticity orthotropic parameters. By choosing the preferred directions as $\mathbf{n}_1=[1,0,0]^T$ and $\mathbf{n}_2=[0,1,0]^T$, the new elastic orthotropic constants can be defined as follows

$$\begin{aligned}&\lambda=\mathfrak{c}_{33}+2(\mathfrak{c}_{44}-\mathfrak{c}_{55}-\mathfrak{c}_{66})\mu=\mathfrak{c}_{55}+\mathfrak{c}_{66}-\mathfrak{c}_{44}o_1=\mathfrak{c}_{11}+\mathfrak{c}_{33}-4\mathfrak{c}_{55}-2\mathfrak{c}_{13}o_2=\mathfrak{c}_{22}+\mathfrak{c}_{33}-\\&4\mathfrak{c}_{66}-2\mathfrak{c}_{23}o_3=\mathfrak{c}_{44}-\mathfrak{c}_{66}o_4=\mathfrak{c}_{44}-\mathfrak{c}_{55}o_5=\mathfrak{c}_{13}-\mathfrak{c}_{33}-2(\mathfrak{c}_{44}-\mathfrak{c}_{55}-\mathfrak{c}_{66})o_6=\mathfrak{c}_{23}-\mathfrak{c}_{33}\\&-2(\mathfrak{c}_{44}-\mathfrak{c}_{55}-\mathfrak{c}_{66})o_7=\mathfrak{c}_{12}-\mathfrak{c}_{13}-\mathfrak{c}_{23}+\mathfrak{c}_{33}+2(\mathfrak{c}_{44}-\mathfrak{c}_{55}-\mathfrak{c}_{66})\end{aligned} \tag{43}$$

3.5. Orthotropic yield criterion

The aim of yield function formulation is to model plastic anisotropy by using the structural tensors defined in terms of isotropic function of the material symmetry group ϑ. In the proposed formulation, the orthotropic yield function is defined using the classical Hill's yield criterion [29]. The hardening is modelled as an isotropic hardening. Therefore, the yield surface is expected to maintain its initial shape (change in size, not shape). The yield surface expansion is controlled by the physically and a thermally micromechanical-based model–Mechanical Threshold Stress (MTS) model [24].

The dependence on material anisotropy during plastic deformation is modelled by the introduction of the structural tensors $\hat{\mathbf{M}}_{ii}|i=1,2,3$ with respect to the isoclinic configuration $\hat{\boldsymbol{\Omega}}_i$. The corresponding yield surface is defined in a new deviatoric plane as a result of the new stress tensor decomposition. Using the symmetric Mandel stress tensor defined in Eq. (24), the yield function can be written as

$$\hat{f}=\hat{f}\ (\hat{\boldsymbol{\Sigma}}',\boldsymbol{\alpha}) \tag{44}$$

where α is an isotropic hardening variable. The properties of symmetric orthotropy are considered by introducing the structural tensors, $\hat{\mathbf{M}}_{ii}$ as follows:

$$\hat{f}=\hat{f}\ (\hat{\boldsymbol{\Sigma}}',\hat{\mathbf{M}}_{ii},\ \boldsymbol{\alpha}) \tag{45}$$

Accordingly, the plastic anisotropy of the new constitutive model is characterized by Hill's anisotropy yield function as follows:

$$\hat{f}=\sqrt{\hat{\boldsymbol{\Sigma}}':\hat{\mathbb{h}}:\hat{\boldsymbol{\Sigma}}'}-\hat{f}\ (\boldsymbol{\alpha})=0 \tag{46}$$

where $\hat{\mathbb{h}}$ is a fourth-order tensor defined in the isoclinic configuration $\hat{\boldsymbol{\Omega}}_i$. The dependence of the above yield function on Hill's yield criterion and structural tensors is represented by this tensor. $\hat{f}\ (\alpha)$ in the above equation defines the evolving flow stress that is controlled by isotropic hardening. The Hill's effective stress can be expressed in terms of the deviatoric Mandel stress in the isoclinic configuration $\hat{\boldsymbol{\Omega}}_i$ as follows:

$$\bar{\hat{\boldsymbol{\Sigma}}}'=\sqrt{\frac{3}{2}\left[\frac{\boldsymbol{F}(\hat{\boldsymbol{\Sigma}}'_y-\hat{\boldsymbol{\Sigma}}'_z)^2+\boldsymbol{G}(\hat{\boldsymbol{\Sigma}}'_z-\hat{\boldsymbol{\Sigma}}'_x)^2+\boldsymbol{H}(\hat{\boldsymbol{\Sigma}}'_x-\hat{\boldsymbol{\Sigma}}'_y)^2+2\boldsymbol{L}\hat{\boldsymbol{\Sigma}}'^2_{yz}+2\boldsymbol{M}\hat{\boldsymbol{\Sigma}}'^2_{zx}+2\boldsymbol{N}\hat{\boldsymbol{\Sigma}}'^2_{xy}}{\boldsymbol{F}+\boldsymbol{G}+\boldsymbol{H}}\right]} \tag{47}$$

The fourth-order plastic anisotropy tensor $\hat{\mathbb{h}}$ is characterized by the Hill's matrix:

$$\hat{\mathbb{h}}=\begin{bmatrix} G+H & -H & -G & 0 & 0 & 0 \\ -H & H+F & -F & 0 & 0 & 0 \\ -G & -F & F+G & 0 & 0 & 0 \\ 0 & 0 & 0 & 2N & 0 & 0 \\ 0 & 0 & 0 & 0 & 2L & 0 \\ 0 & 0 & 0 & 0 & 0 & 2M \end{bmatrix} \tag{48}$$

By comparing the Hill's matrix with the fourth-order isotropic tensor function $\hat{\mathbb{M}}$ in Eq. (40) the orthotropic plastic constants $(\lambda,\ \mu,\ o_i|_{i=1,..7})$ are obtained:

$$\lambda=\frac{1}{2}F+\frac{1}{2}G+2(N-L-M)\mu=L+M-No_1=\frac{1}{2}F+\frac{1}{2}H+2G-4Lo_2=\frac{1}{2}G+\frac{1}{2}H+2F-4Mo_3=N-Mo_4=N-Lo_5=-\frac{1}{2}F-G+2L+2M-2No_6=-\frac{1}{2}G-F+2L+2M-2No_7=-\frac{1}{2}H+F+G+2N-2L-2M \tag{49}$$

3.6. The Clausius-Plank inequality

The evolution equations for the specified variables of the new constitutive model are defined with respect to the second law of thermodynamics framework. Using the Clausius-Plank inequality, an isothermal and uniform temperature distribution type of deformations can be expressed as

$$\mathcal{D}=\boldsymbol{S}:\dot{\mathbf{E}}-\dot{\Psi}\geq 0 \tag{50}$$

where $\dot{\Psi}$ is a rate of Helmholtz free energy function, and $\dot{\mathbf{E}}$ is

$$\dot{\mathbf{E}}=\frac{1}{2}\dot{\mathbf{C}} \tag{51}$$

Using Eqs. (51) and (50) can be rewritten as follows:

$$\mathcal{D}=\boldsymbol{S}:\frac{1}{2}\dot{\mathbf{C}}-\dot{\boldsymbol{\Psi}}\geq 0 \tag{52}$$

Considering the free strain energy (Helmholtz free energy) function is represented by the elastic Cauchy-Green strain tensor $\mathbf{C}_e$, and the strain-like internal variable describing isotropic plastic hardening ξ_h, $\Psi=\Psi(\mathbf{C}_e,\ \xi_h)$, this function can be easily divided into elastic and plastic as

$$\boldsymbol{\Psi}=\boldsymbol{\Psi}_e(\mathbf{C}_e)+\boldsymbol{\Psi}_p(\xi_h) \tag{53}$$

The differentiating of the above equation with respect to time leads to

$$\dot{\boldsymbol{\Psi}}=\frac{\partial\boldsymbol{\Psi}_e}{\partial\mathbf{C}_e}:\dot{\mathbf{C}}_e+\frac{\partial\boldsymbol{\Psi}_p}{\partial\xi_h}\bullet\dot{\xi}_h \tag{54}$$

Substituting Eq. (54) into Eq. (52) gives

$$\mathcal{D}=\boldsymbol{S}:\frac{1}{2}\dot{\mathbf{C}}-\left(\frac{\partial\boldsymbol{\Psi}_e}{\partial\mathbf{C}_e}:\dot{\mathbf{C}}_e+\frac{\partial\boldsymbol{\Psi}_p}{\partial\xi_h}\bullet\dot{\xi}_h\right)\geq 0 \tag{55}$$

Using $\mathbf{C}_e=\mathbf{F}_p^{-T}\bullet\mathbf{C}\bullet\mathbf{F}_p^{-1}$ and its material time derivative $\dot{\mathbf{C}}_e=\dot{\mathbf{F}}_p^{-T}\bullet\mathbf{C}\bullet\mathbf{F}_p^{-1}+\mathbf{F}_p^{-T}\bullet\dot{\mathbf{C}}\bullet\mathbf{F}_p^{-1}+\mathbf{F}_p^{-T}\bullet\mathbf{C}\bullet\dot{\mathbf{F}}_p^{-1}$, the Mandel stress tensor can be expressed as:

$$\boldsymbol{\Sigma}=\mathbf{C}\bullet\boldsymbol{S}=(\mathbf{F}_p^{T}\bullet\mathbf{C}_e\bullet\mathbf{F}_p)\bullet\left(2\bullet\mathbf{F}_p^{-T}\bullet\frac{\partial\boldsymbol{\Psi}_e}{\partial\mathbf{C}_e}\bullet\mathbf{F}_p^{-1}\right)=2\bullet\mathbf{C}_e\bullet\frac{\partial\boldsymbol{\Psi}_e}{\partial\mathbf{C}_e} \tag{56}$$

Using Eq. (56), the non-negative of the internal dissipation can finally be defined as follows:

$$\mathcal{D}=\boldsymbol{\Sigma}:\mathbf{L}_p-\frac{\partial\boldsymbol{\Psi}_p}{\partial\xi_h}\bullet\dot{\xi}_h\geq 0 \tag{57}$$

The evolution equations for the plastic strain tensors are derived based on the principle of maximum plastic dissipation. In addition, the normality rules gives function of $\mathbf{L}_p$ and $\dot{\xi}_h$ as

$$\mathbf{L}_p=\dot{\lambda}\frac{\partial f}{\partial\boldsymbol{\Sigma}'},\ \dot{\xi}_h=\dot{\lambda}\frac{\partial f}{\partial\boldsymbol{\alpha}} \tag{58}$$

These equations satisfy the associative flow rule and the expression for evolution equation, respectively. Equally $\dot{\xi}_h$ is a work conjugate of the stress-like internal variable describing isotropic hardening α. Finally the local dissipation inequality can be expressed with respect to the isoclinic configuration $\hat{\boldsymbol{\Omega}}_i$ as

$$\hat{\mathcal{D}}=\hat{\boldsymbol{\Sigma}}':\hat{\mathbf{L}}_p-\boldsymbol{\alpha}:\dot{\xi}_h\geq 0 \tag{59}$$

where

$$\widehat{\mathbf{L}_P}=\dot{\lambda}\frac{\partial\hat{f}}{\partial\hat{\Sigma}'},\ \dot{\xi}_h=\dot{\lambda}\frac{\partial\hat{f}}{\partial\boldsymbol{\alpha}} \tag{60}$$

Since the Mandel stress adopted in the formulation is symmetric and because this stress measure is thermodynamically conjugate to the plastic velocity gradient, only the symmetric part of the plastic velocity gradient is adopted in the formulation. Therefore, in this work, the plastic spin is assumed vanish in the chosen isoclinic configuration. Using symmetry of Mandel stress and assuming that the plastic spin is equal to zero in the isoclinic configuration $\hat{\boldsymbol{\Omega}}_i$, Eq. (59) can be rewritten as

$$\hat{\mathcal{D}}=\hat{\boldsymbol{\Sigma}}':\mathbf{sym}\hat{\mathbf{L}}_p-\boldsymbol{\alpha}:\dot{\xi}_h\geq 0 \tag{61}$$

The above expression is also written as

$$\hat{\mathcal{D}}=\hat{\boldsymbol{\Sigma}}':\hat{\mathbf{D}}_p-\boldsymbol{\alpha}:\dot{\xi}_h\geq 0 \tag{62}$$

A similar approach has been adopted in [20], in contrast to the concept used by [61–63] that define a so-called plastic material spin. By using the yield function Eq. (46) in the first part of Eq. (60), the evolution of the plastic deformation $\hat{\mathbf{D}}_p$ can be expressed as follows:

$$\hat{\mathbf{D}}_p=\dot{\lambda}\frac{(\hat{\mathbb{h}}\bullet\hat{\boldsymbol{\Sigma}}'+(\hat{\mathbb{h}}\bullet\hat{\boldsymbol{\Sigma}}')^{T}+\hat{\mathbb{h}}^{T}\bullet\hat{\boldsymbol{\Sigma}}'+(\hat{\mathbb{h}}^{T}\bullet\hat{\boldsymbol{\Sigma}}')^{T})}{4\sqrt{\hat{\boldsymbol{\Sigma}}':\hat{\mathbb{h}}:\hat{\boldsymbol{\Sigma}}'}} \tag{63}$$

Therefore, the inequality of dissipation energy in Eq. (62) can be expressed as follows:

$$\hat{\mathcal{D}}=\hat{\boldsymbol{\Sigma}}'\bullet\left[\dot{\lambda}\frac{(\hat{\mathbb{h}}\bullet\hat{\boldsymbol{\Sigma}}'+(\hat{\mathbb{h}}\bullet\hat{\boldsymbol{\Sigma}}')^{T}+\hat{\mathbb{h}}^{T}\bullet\hat{\boldsymbol{\Sigma}}'+(\hat{\mathbb{h}}^{T}\bullet\hat{\boldsymbol{\Sigma}}')^{T})}{4\sqrt{\hat{\boldsymbol{\Sigma}}':\hat{\mathbb{h}}:\hat{\boldsymbol{\Sigma}}'}}\right]-\boldsymbol{\alpha}:\dot{\xi}_h\geq 0 \tag{64}$$

Using the above identities, eventually the Clausius-Plank inequality of the second law of thermodynamics for the new constitutive model can be expressed with respect to the isoclinic configuration $\hat{\boldsymbol{\Omega}}_i$ as follows:

$$\hat{\mathcal{D}}=\dot{\lambda}\left(\sqrt{\hat{\boldsymbol{\Sigma}}':\hat{\mathbb{h}}:\hat{\boldsymbol{\Sigma}}'}-\boldsymbol{\alpha}:\frac{\partial f}{\partial\boldsymbol{\alpha}}\right)\geq 0 \tag{65}$$

3.7. Plastic flow rule of the new constitutive model

The evolution equation which determines the relation between the stress and strain increments of the constitutive relations is defined from the consistency condition. Let us first write the plastic velocity gradient $\hat{\mathbf{L}}_p$ in the isoclinic configuration $\hat{\boldsymbol{\Omega}}_i$ as

$$\hat{\mathbf{L}}_p=\dot{\hat{\mathbf{F}}}_p\bullet\hat{\mathbf{F}}_p^{-1}=\dot{\lambda}\hat{\mathbf{r}}(\hat{\boldsymbol{\Sigma}}',\ \alpha) \tag{66}$$

The plastic flow direction is marked by $\hat{\mathbf{r}}$ and set equal to $\frac{\partial\hat{f}}{\partial\hat{\boldsymbol{\Sigma}}'}$. Further, the evolution of isotropic hardening law is given by

$$\dot{\alpha}=\dot{\lambda}\hat{\mathbf{H}}(\hat{\boldsymbol{\Sigma}}',\alpha) \tag{67}$$

where $\hat{\mathbf{H}}$ represents the plastic modulus that is defined from the referential curves of the MTS model. By using the yield function Eq. (45), the loading-unloading condition and considering the structural tensors remain constant in the isoclinic configuration, $\dot{\hat{\mathbf{M}}}_{ii}=0$, the

consistency condition of the new constitutive model can be defined as

$$\dot{\hat{f}} = \hat{f}_{\hat{\Sigma}} : \dot{\hat{\Sigma}}' + \hat{f}_{\alpha} \bullet \dot{\alpha} = 0 \tag{68}$$

where

$$\hat{f}_{\hat{\Sigma}'} = \frac{\partial \hat{f}}{\partial \hat{\Sigma}'} \hat{f}_{\alpha} = \frac{\partial \hat{f}}{\partial \alpha} \tag{69}$$

Using $\bar{\hat{\Sigma}}' = \sqrt{\frac{3}{2}(\hat{\Sigma}' \hat{\mathbb{h}})^T \hat{\Sigma}'}$ to define the orthotropic yield criterion, $\hat{f}(\alpha)$ in Eq. (46) can be re written as

$$\hat{f}(\boldsymbol{\alpha}) = \sqrt{\frac{2}{3}} \bar{\hat{\Sigma}}' \tag{70}$$

The rate of this expression $\dot{\alpha}$ can be expressed as

$$\dot{\boldsymbol{\alpha}} = \sqrt{\frac{2}{3}} \dot{\bar{\hat{\Sigma}}}' \tag{71}$$

where $\dot{\bar{\hat{\Sigma}}}'$ is given by

$$\dot{\bar{\hat{\Sigma}}}' = \hat{\mathbf{H}} \bar{\hat{\mathbf{D}}}_p \tag{72}$$

Combining Eqs. (71) and (72) results in

$$\dot{\alpha} = \sqrt{\frac{2}{3}} \hat{\mathbf{H}} \bar{\hat{\mathbf{D}}}_p \tag{73}$$

Subsequently, simplifying $\sqrt{\frac{2}{3}}\hat{\mathbf{H}}$ as $\hat{\mathbf{K}}_f$ and defining $\bar{\hat{\mathbf{D}}}_p = \sqrt{\frac{2}{3}}\dot{\lambda}$, the above equation can be rewritten as

$$\dot{\boldsymbol{\alpha}} = \dot{\boldsymbol{\lambda}} \sqrt{\frac{2}{3}} \hat{\mathbf{K}}_f \tag{74}$$

Using this equation, the consistency condition of the new constitutive model Eq. (68) can be re expressed as

$$\dot{\hat{f}} = \hat{f}_{\hat{\Sigma}'} : \dot{\hat{\Sigma}}' + \hat{f}_{\alpha} \bullet \dot{\lambda} \sqrt{\frac{2}{3}} \hat{\mathbf{K}}_f = 0 \tag{75}$$

The formulation of the plastic flow equation in the intermediate configuration requires the decomposition of the deformation rate into elastic and plastic parts. The formulation however differs between hyperelastic-plastic materials defined in this work and hypoelastic-plastic materials when the plastic flow equation is specified in terms of plastic velocity gradient $\hat{\mathbf{L}}_p$ as shown in Eq. (66), [10]. Subsequently, using $\dot{\hat{\Sigma}}' = \frac{\partial^2 \hat{\Psi}}{\partial \hat{\mathbf{E}}_e \partial \hat{\mathbf{E}}_e} : \dot{\hat{\mathbf{E}}}_e = \mathbf{C}_{el}^{\hat{\Sigma}p} : \dot{\hat{\mathbf{E}}}_e = \mathbf{C}_{el}^{\hat{\Sigma}p} : (\hat{\mathbf{D}} - \hat{\mathbf{D}}_p)$ in the above equation where $\mathbf{C}_{el}^{\hat{\Sigma}p} = \frac{\partial^2 \hat{\Psi}}{\partial \hat{\mathbf{E}}_e \partial \hat{\mathbf{E}}_e}$ refers to the elasticity tensor (material stiffness tensor) that relates the material time derivative of the Mandel stress $\dot{\hat{\Sigma}}'$ to the material time derivative of the Green strain $\dot{\hat{\mathbf{E}}}_e$ in the isoclinic configuration $\hat{\boldsymbol{\Omega}}_i$, the consistency condition of the proposed formulation in the isoclinic configuration $\hat{\boldsymbol{\Omega}}_i$ can be further derived as follows:

$$\dot{\hat{f}} = \hat{f}_{\hat{\Sigma}'} : \mathbf{C}_{el}^{\hat{\Sigma}p} : (\hat{\mathbf{D}} - \hat{\mathbf{D}}_p) + \hat{f}_{\alpha} \bullet \dot{\lambda} \sqrt{\frac{2}{3}} \hat{\mathbf{K}}_f \tag{76}$$

Introducing $\hat{\mathbf{D}}_p$ equals to $\mathrm{sym}\hat{\mathbf{L}}_p = \dot{\lambda}\mathrm{sym}\hat{\mathbf{r}}$ in the above equation, [10], the plastic rate parameter $\dot{\lambda}$ can be expressed as

$$\dot{\lambda} = \frac{\hat{f}_{\hat{\Sigma}'} : \mathbf{C}_{el}^{\hat{\Sigma}p} : \hat{\mathbf{D}}}{-\hat{f}_{\alpha} \bullet \sqrt{\frac{2}{3}} \hat{\mathbf{K}}_f + \hat{f}_{\hat{\Sigma}'} : \mathbf{C}_{el}^{\hat{\Sigma}p} : \mathbf{sym}\hat{\mathbf{r}}} \tag{77}$$

3.8. The Elasto-Plastic tangent modulus

The plastic rate parameter $\dot{\lambda}$ can be used to explicitly define the relation between the stress and strain increments of the new constitutive model in the isoclinic configuration $\hat{\boldsymbol{\Omega}}_i$ within elastic and plastic regimes using the following equation:

$$\dot{\hat{\Sigma}}' = \mathbf{C}_{el}^{\hat{\Sigma}p} : (\hat{\mathbf{D}} - \hat{\mathbf{D}}_p) = \mathbf{C}_{el}^{\hat{\Sigma}p} : (\hat{\mathbf{D}} - \dot{\boldsymbol{\lambda}} \mathbf{sym}\hat{\mathbf{r}}) \tag{78}$$

Using Eq. (77), this equation can be further written as follows:

$$\dot{\hat{\Sigma}}' = \mathbf{C}_{el}^{\hat{\Sigma}p} : \left(\hat{\mathbf{D}} - \frac{\hat{f}_{\hat{\Sigma}'} : \mathbf{C}_{el}^{\hat{\Sigma}p} : \hat{\mathbf{D}}}{-\hat{f}_{\alpha} \bullet \sqrt{\frac{2}{3}} \hat{\mathbf{K}}_f + \hat{f}_{\hat{\Sigma}'} : \mathbf{C}_{el}^{\hat{\Sigma}p} : \mathbf{sym}\hat{\mathbf{r}}} \mathbf{sym}\hat{\mathbf{r}} \right) \tag{79}$$

Finally, with some arrangements the relationship between the stress and strain increments within elastic and plastic regimes in $\hat{\boldsymbol{\Omega}}_i$ is concluded by the elasto-plastic tangent modulus $\mathbf{C}_{\hat{\Sigma}'}$;

$$\mathbf{C}_{\hat{\Sigma}'} = \mathbf{C}_{el}^{\hat{\Sigma}'} - \frac{(\mathbf{C}_{el}^{\hat{\Sigma}p} : \mathbf{sym}\hat{\mathbf{r}}) \otimes (\hat{f}_{\hat{\Sigma}'} : \mathbf{C}_{el}^{\hat{\Sigma}p})}{-\hat{f}_{\alpha} \bullet \sqrt{\frac{2}{3}} \hat{\mathbf{K}}_f + \hat{f}_{\hat{\Sigma}'} : \mathbf{C}_{el}^{\hat{\Sigma}p} : \mathbf{sym}\hat{\mathbf{r}}} \tag{80}$$

4. Validation and results

The proposed formulations in the preceding sections are implemented into the LLNL-DYNA3D and named Material Type 93. On the completion of the implementation process, the capability of the new constitutive model to capture strain rate and temperature sensitivities of orthotropic materials is first checked. The numerical simulation results of the newly proposed constitutive model are then compared against the published experimental data of Plate Impact and Taylor Cylinder Impact Tests *A* cm−g−μs *units system is adopted in the involved numerical tests.*

4.1. Strain rate and temperature dependency tests

To investigate rate sensitivity and temperature sensitivity of the new constitutive model, a series of one element analyses are performed. The single element with the node numbering used to define boundary conditions is shown in Fig. 4. Assuming the single element represents one of the elements around the gauge length of the uniaxial stress test's specimen, the uniform plastic deformation observed in the element is applicable to predict strain rate and temperature dependent using this simplified analysis. Bear in mind that this comparison method is only valid for the test data before the plastic deformation occurs non-uniformly (localisation or necking) in the test specimen.

In this model the principal directions of material orthotropy are aligned with the x, y, z axis of the global coordinate system. The displacement boundary conditions applied in these tests are summarised in Table 1. Loading in tension is applied to the elements by

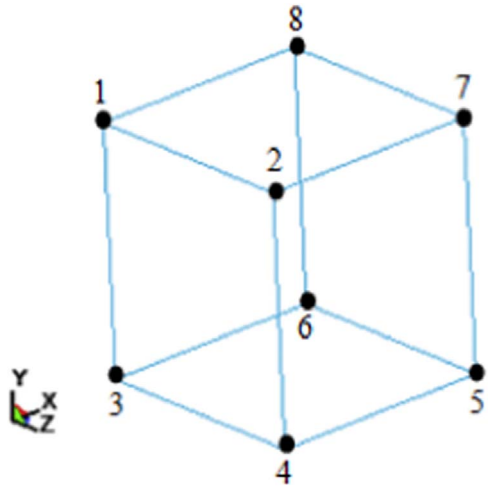

Fig. 4. Single element configuration.

Table 1
Displacements boundary condition for a uniaxial stress and uniaxial strain tests in the x direction.

Node number	Displacement boundary condition of uniaxial stress
1	No constraints
2	No constraints
3	No constraints
4	No constraints
5	Constrained x, y and z displacements
6	Constrained x displacement
7	Constrained x displacement
8	Constrained x displacement

Table 2
Aluminium 7010 material parameters for elastic-plastic with isotropic plastic hardening analysis.

Material properties	Value
Young's modulus	
E_a	70.06 GPa
E_b	71.1 GPa
E_c	70.6 GPa
Poisson's ratio	
v_{ba}	0.342
v_{ca}	0.342
v_{cb}	0.342
Shear modulus	
G_{bc}	26.3 GPa
G_{ab}	26.5 GPa
G_{ac}	26.5 GPa
Yield stress in a − direction	
σ_y	504 MPa
Tangent plastic modulus in a − direction	
H	0.65 GPa
Hill's parameters	
R	0.836
P	0.824
Q_{bc}	1
Q_{ba}	1
Q_{ca}	1.0377

prescribing displacement load curves to nodes 1, 2, 3 and 4.

The tensile test data of Aluminium 7010 published in [56] is used in this validation stage. The parameters defined for this specimen are given in Tables 2 and 3.

The stress-strain curves for quasi-static tension tests ($6.4x10^{-4}$ s^{-1}strain rate) conducted at −50 °C and 70 °C are presented in Fig. 5. In addition, Fig. 6 shows the stress-strain curves of the specimen tested at 140 °C at two different strain rates; $6.4x10^{0}$ s^{-1} and $6.4x10^{-1}$ s^{-1}. It can be clearly seen from these figures that the specimen exhibits strain rate and temperature sensitivity.

The strain rate and temperature predictions of the newly constitutive model are shown in the following figures.

Figs. 7–10 show that the flow stress (MTS model) of the new constitutive model shows a good agreement with the rate and temperature sensitivity of the specimen. The flow stress formulated as a function of the microstructural state has captured a reasonable relationship between stress, strain rate and temperature of Aluminium 7010. Small variances between the simulation and the experimental results might be caused by the MTS properties used to control the flow stress of the new constitutive model.

It can be concluded that increasing strain rate increases the flow stress, while increasing temperature decreases the flow stress. In other words, the saturation stress of the new formulation increases with increasing strain rate and decreases with increasing temperature.

Table 3
MTS parameters of aluminium 7010.

Parameter	Description	Value
$\hat{\sigma}_a$	Athermal threshold stress	100 MPa
$\hat{\sigma}_0$	Initial threshold stress	600 MPa
$g_{0\varepsilon s}$	Normalized activation energy	1.606
$\dot{\varepsilon}_{s0}$	Reference strain rate	$1.0x10^{7}$ s^{-1}
b	Magnitude of the Burgers' vector	$0.286x10^{-9}$ m
k_b	Boltzmann constant	$1.36x10^{-23}$ J/K
$p_{\dot{\varepsilon}}$	Free energy equation exponent	1
$q_{\dot{\varepsilon}}$	Free energy equation exponent	1
A	Saturation stress constant	5.542
$\hat{\sigma}_{\dot{\varepsilon}s0}$	Saturation threshold stress at 0 K	801.01 MPa
$\dot{\varepsilon}_{s0}$	Reference strain rate of saturation threshold stress	$1.0x10^{7}s^{-1}$
a_0	Constant of hardening function	67604.6 MPa
a_1	Constant of hardening function	1816.9 MPa
a_2	Constant of hardening function	202.3 MPa
b_0	Shear modulus at 0 K	28.83 GPa
b_1	Shear modulus constant	4.45 GPa
b_2	Shear modulus constant	248.5 K
T_r	Reference temperature	293.15 K
ρ	Density	2.81 g cm^{-3}
C_p	Heat capacity	896 J/kg K

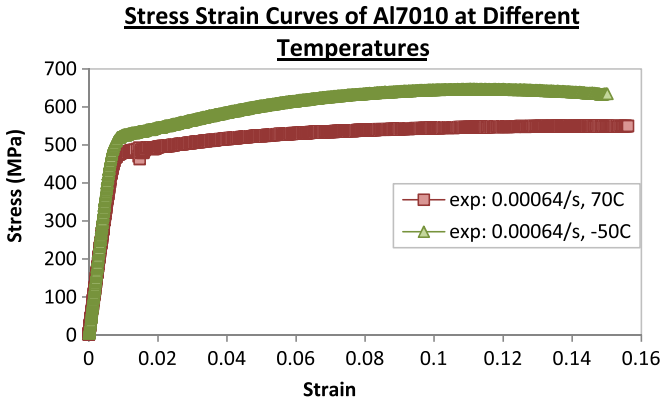

Fig. 5. Stress Strain Curves of Aluminium 7010 at $6.4x10^{-4}$ s^{-1} at different temperatures.

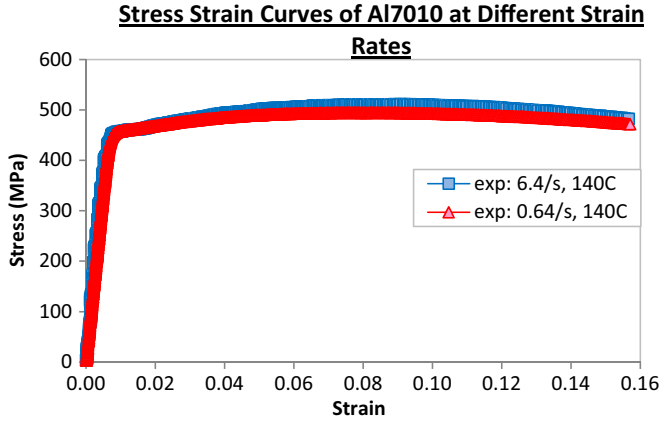

Fig. 6. Stress strain curves of Aluminium 7010 at 140 °C at different strain rates.

4.2. Plate impact test analysis of aluminium alloy 7010

The capability of the newly implemented constitutive model to represent the behaviour of orthotropic metals when impacted with shock loading at high impact velocity is investigated in this stage. Fig. 11 shows the configuration of the Plate Impact test simulation.

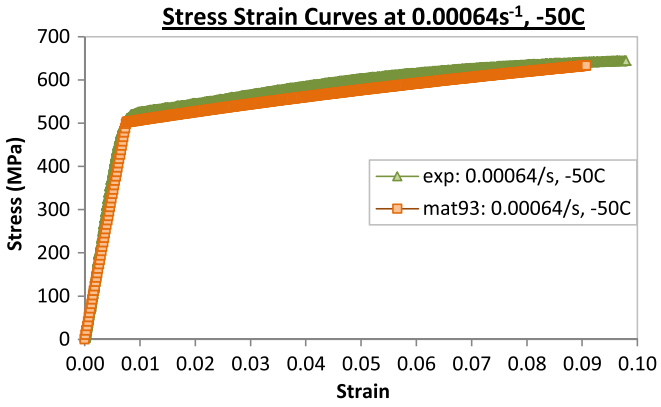

Fig. 7. Stress strain curves comparison between Mat93 and experimental data at $6.4x10^{-4}$ s^{-1}, −50 °C.

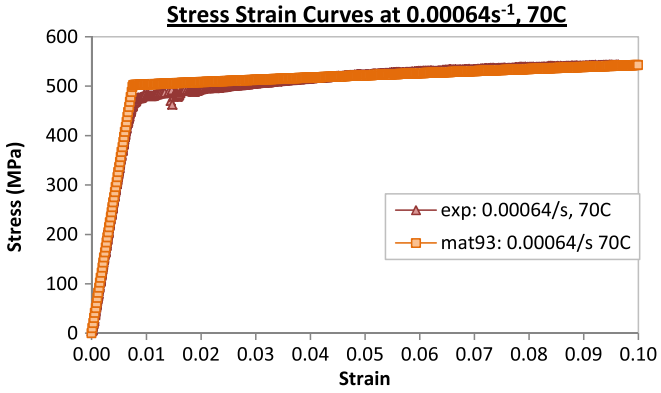

Fig. 8. Stress strain curves comparison between Mat93 and experimental data at $6.4x10^{-4}$ s, 70 °C.

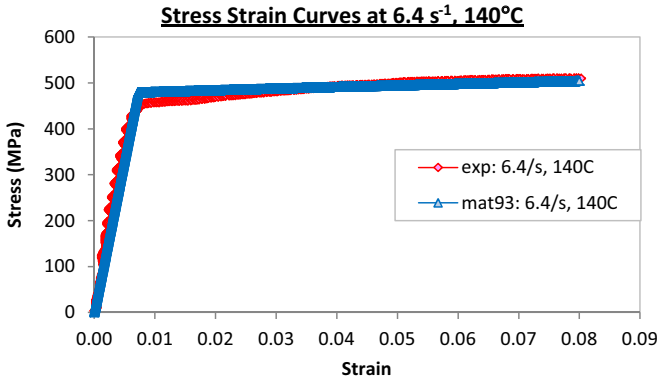

Fig. 9. Stress strain curves comparison between Mat93 and experimental data at $6.4x10^{-4}$ s, 140 °C.

It can be observed that the test consists of three parts of rectangular bars with 4*x*4 solid elements for its cross section (*XY* plane). The first bar represents the PMMA block, while the second and third bars refer to the test specimen and flyer respectively. The mesh of this simulation is set to allow a 1D wave to propagate along the length of the bars when the impact happens. From this figure, it is noticed that symmetrical planes are adopted on all sides of the bars.

To ensure that no release wave is reflected from the back of the PMMA block into the test specimen, a non-reflecting boundary condition is applied to the back of this block (PMMA). In addition, the flyer, test specimen and PMMA bars are modelled with 25 solid elements (2.5 mm in length), 75 solid elements (10 mm in length) and 100 solid elements (12 mm in length) respectively, parallel to the impact axis (*Z* axis). A contact interface is defined in between the flyer

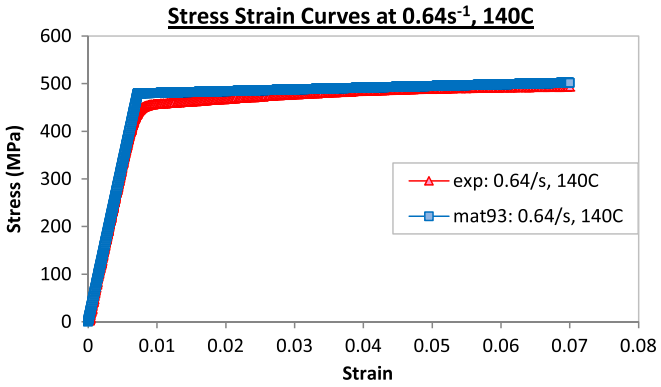

Fig. 10. Stress strain curves comparison between Mat93 and experimental data at $6.4x10^{-4}$ s, 140 °C.

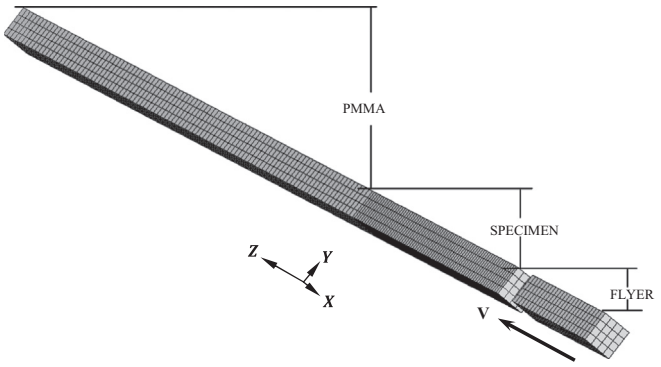

Fig. 11. Configuration of the plate impact test simulation.

and the test specimen. To record the stress time histories of the impact, a time history block is defined in the elements at the top of PMMA bar.

In this analysis, the longitudinal stress (Z stress) in the elements at the top of the PMMA bar is compared with the experimental data with respect to the short transverse and the longitudinal (rolling) directions of the specimen. The MTS flow stress is excluded at this stage of validation. The material properties used in this analysis are shown in Table 4.

The flyer is defined as Aluminium 6082−T6. Both the flyer and the PMMA blocks are assigned with DYNA3D's Material Type 10 (Isotropic-Elastic-Plastic-Hydrodynamic). The Gruneisen equation of state is adopted to appropriately represent the shock loading developed in this test. In addition, three different impact velocities are performed in these analyses 234 ms^{-1}, 450 ms^{-1} and 895 ms^{-1}. By setting the material axes definition as AOPT 2 (globally orthotropic), the following results are obtained:

It can be observed in Figs. 12–17 that the elastic-plastic loading-unloading behaviours of the Al7010 are well captured by the proposed constitutive model. A slope that is developed in the initial increment of the longitudinal stress represents the Hugoniot Elastic Limit (HEL). Without knowing the error that might happen in the experimental test, such as an inaccuracy of the gauge used to measure the longitudinal stress etc., a slight difference between the new constitutive model's HEL and the values obtained experimentally is acceptable. In addition, a different HEL value obtained in each direction is a sign of an adequate anisotropy level of the material under consideration.

The width of the generated pulses in each analysis is reasonably agreed with the experimental test data. Furthermore, very close Hugoniot stress levels between the new constitutive model and the experimental data proved the capability of the newly implemented orthotropic pressure to capture shockwaves in orthotropic materials. The comparison between Material Type 93 and the experimental results are analyzed and summarised in Table 5.

In this analysis, it can be clearly seen that the tensile wave failure or

Table 4
Material properties for plate impact test analysis.

Parameters	Al7010	Al6082	PMMA
E_a	70.6 GPa	–	–
E_b	71.1 GPa	–	–
E_c	70.6 GPa	–	–
ν_{ba}	0.342	–	–
ν_{ca}	0.342	–	–
ν_{cb}	0.342	–	–
G_{bc}	26.31 GPa	26.8 GPa	2.3 GPa
G_{ab}	26.48 GPa	26.8 GPa	2.3 GPa
G_{ac}	26.48 GPa	26.8 GPa	2.3 GPa
σ_y	564 MPa	250 MPa	70 MPa
H	0.13 GPa	130 GPa	300 MPa
P_{cut}	–	2.5 GPa	–
ρ	2.81 g cm^{-3}	2.7 g cm^{-3}	1.18 g cm^{-3}
Hill's parameters			
R	1	–	–
P	0.719	–	–
Q_{bc}	1	–	–
Q_{ba}	1	–	–
Q_{ca}	1	–	–
Gruneisen parameters			
C	5200 ms^{-1}	5240 ms^{-1}	2180 ms^{-1}
s_1	1.36	1.4	2.088
s_2	0.00	0.00	−1.124
s_3	0.00	0.00	0.00
Γ	2.2	1.97	0.85
A	0.48	0.48	0.00

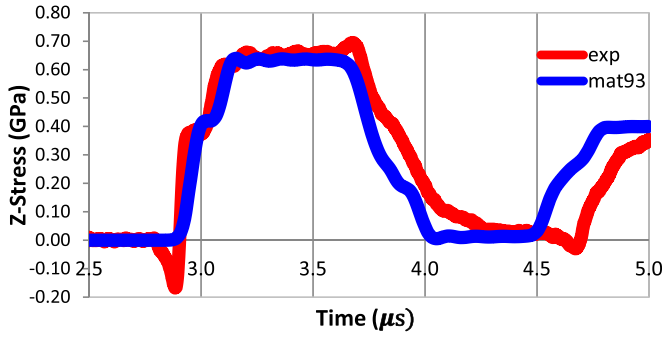

Fig. 12. Longitudinal stress (Z stress) comparison at 234 ms^{-1} in longitudinal direction.

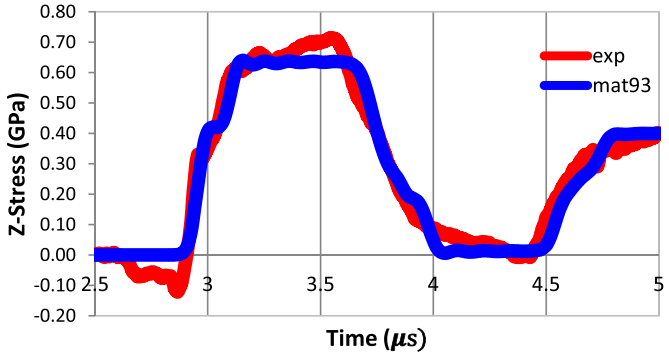

Fig. 13. Longitudinal stress (Z stress) comparison at 234 ms^{-1} in transverse direction.

spall (demonstrated by the reloading of the longitudinal stress after the first loading-unloading pulse) is not generated in the specimen when impacted with a lower impact velocity (234 ms^{-1}). However, a clear spall criterion can be observed when higher impact velocities (450 ms^{-1} and 895 ms^{-1}) are applied. Such behaviour could not be captured by the Material Type 93 due to the absence of damage and failure models in the proposed formulation of this constitutive model.

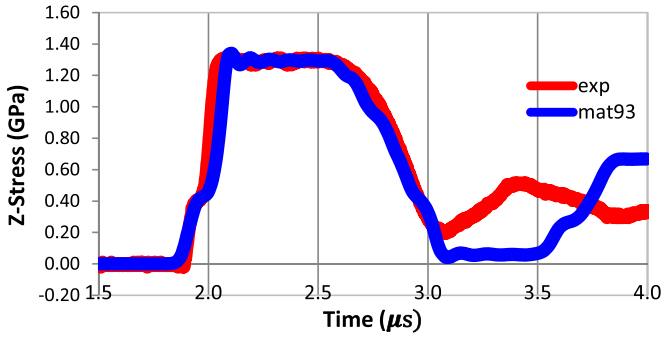

Fig. 14. Longitudinal stress (Z stress) comparison at 450 ms^{-1} in longitudinal direction.

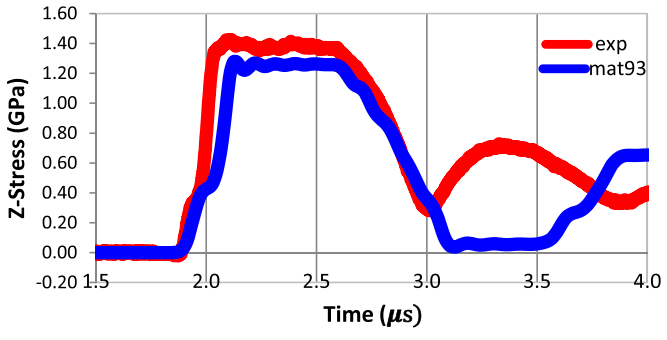

Fig. 15. Longitudinal stress (Z Stress) comparison at 450 ms^{-1} in transverse direction.

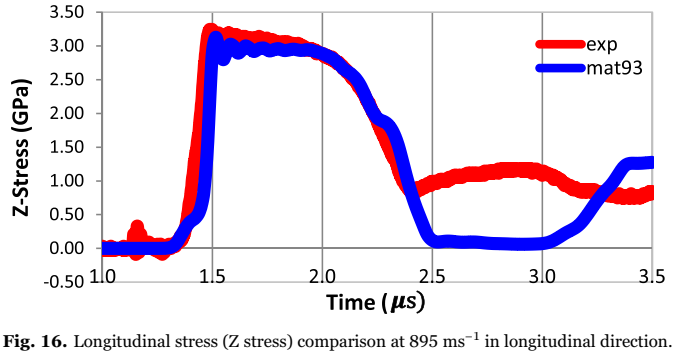

Fig. 16. Longitudinal stress (Z stress) comparison at 895 ms^{-1} in longitudinal direction.

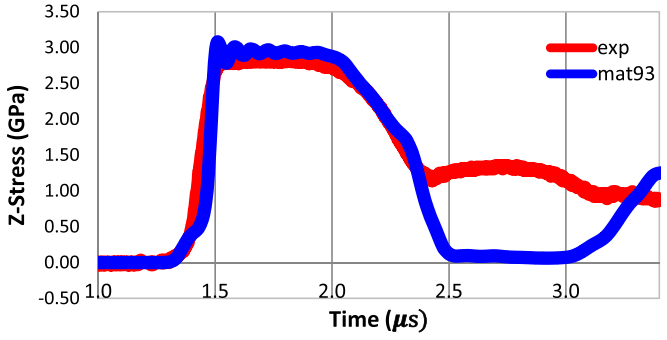

Fig. 17. Longitudinal stress (Z stress) comparison at 895 ms^{-1} in transverse direction.

4.3. Taylor cyliner impact test analysis of aluminium alloy 7010

The capability of the new constitutive model to represent the deformation behaviour of orthotropic metals within a three-dimensional stress state is accessed in this section. A standard configuration of this simulation test is depicted by Fig. 18.

It can be observed that this test creates an impact between a solid cylinder rod of material (specimen) and a fixed rigid surface (anvil) as a target. Strictly speaking, a cylindrical rod is fired into a fixed rigid plate at high velocity (left). This impact subsequently produces permanent

Table 5
Comparison results of plate impact test.

Impact Velocity/Direction	Analysis Criteria		
	HEL (GPa)	Hugoniot Stress Level (GPa)	Pulse (μs)
234 ms^{-1} (Longitudinal)			
Simulation	0. 41	0. 64	1. 15
Experiment	0. 39	0. 65	1. 40
234 ms^{-1} (Transverse)			
Simulation	0. 42	0. 64	1. 15
Experiment	0. 33	0. 70	1. 50
450 ms^{-1} (Longitudinal)			
Simulation	0. 40	1. 28	1. 20
Experiment	0. 40	1. 28	1. 25
450 ms^{-1} (Transverse)			
Simulation	0. 40	1. 28	1. 20
Experiment	0. 34	1. 36	1. 15
895 ms^{-1} (Longitudinal)			
Simulation	0. 35	3. 15	1. 20
Experiment	0. 20	3. 25	1. 10
895 ms^{-1} (Transverse)			
Simulation	0. 35	2. 90	1. 20
Experiment	0. 19	2. 80	1. 10

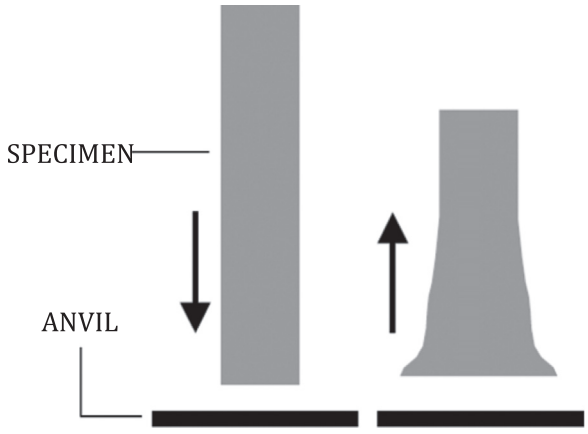

Fig. 18. Diagram of Taylor cylinder Impact test.

deformations in the rebounded cylinder (right). The impact at the bottom end of the cylinder happens at a very high strain rate within a three-dimensional stress state and forms a mushroom-shape around the impact area. The higher amplitude of the velocity impact results in a greater mushrooming of the cylinder.

The FE model used to examine capability of the proposed formulation to represent the deformation behaviour of orthotropic metals within a three-dimensional stress state (3D mode) is shown in Fig. 19. In order to reduce the simulation time of this experimental test, the number of elements to model the cylinder is reduced by modelling a quarter of the cylinder with 9.30 mm diameter and 46.50 mm length. Furthermore, the cylinder is modelled by using a butterfly mesh method with 6375 solid elements, as depicted in this figure. The anvil is modelled as a rigid wall, therefore the impact-interface friction between the solid cylinder rod and the anvil is negligible. 200 ms^{-1} impact velocity is used in this analysis. The material parameters of Aluminium 7010, the Gruneisen EOS and the MTS parameters are given in Tables 6–8 respectively.

In this analysis, the final radius and length of the deformed cylinder profile obtained experimentally are compared with the results generated by new constitutive model. The analysis is simulated until 120 μs to ensure the final deformed shape of the cylinder profile is really obtained. Again, the material axes definition is set as global orthotropic (AOPT 2). Fig. 20 shows the deformation behaviour predicted by the new constitutive model at 5 μs, 20 μs and 50 μs.

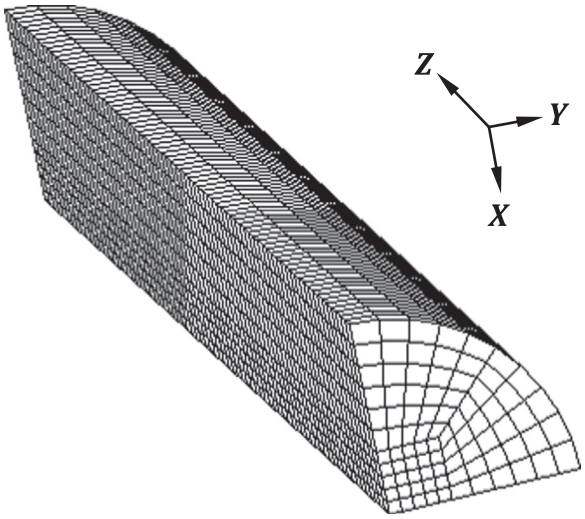

Fig. 19. FE model used to simulate Taylor cylinder Impact test.

Table 6
Aluminium material properties for Taylor cylinder impact test analysis.

Material properties	Value
Young's modulus	
E_a	70.326 GPa
E_b	70.326 GPa
E_c	70.326 GPa
Poisson's ratio	
v_{ba}	0.33
v_{ca}	0.33
v_{cb}	0.33
Shear modulus	
G_{bc}	26.889 GPa
G_{ab}	26.889 GPa
G_{ac}	26.889 GPa
Yield stress in a − direction	
σ_y	504 MPa
Tangent plastic modulus in a − direction	
H	0.65 GPa
Hill's parameters	
R	0.836
P	0.824
Q_{bc}	1
Q_{ba}	1
Q_{ca}	1.0377

Table 7
Gruneisen equation of state parameters.

Parameter	Value
C	5200 ms^{-1}
s_1	1.36
s_2	0.00
s_3	0.00
Γ	2.2
A	0.48

First of all, it can be clearly seen that a mushroom-shape is developed in the deformed cylinders near to the impact area. This is due to the plastic compressive wave that exceeded the yield strength of the specimen being generated in the cylinder. Greater mushrooming is therefore expected for the case where the cylinder is impacted with a

Table 8
MTS parameters of aluminium 7010.

Parameter	Description	Value
$\hat{\sigma}_a$	Athermal threshold stress	10.0 MPa
$\hat{\sigma}_0$	Initial threshold stress	600 MPa
$g_{0\varepsilon s}$	Normalized activation energy	1.606
$\dot{\varepsilon}_{s0}$	Reference strain rate	$1.0x10^{7}$ s^{-1}
b	Magnitude of the Burgers' vector	$0.286x10^{-9}$ m
k_b	Boltzmann constant	$1.36x10^{-23}$ J/K
p_e	Free energy equation exponent	1
q_e	Free energy equation exponent	1
A	Saturation stress constant	5.542
$\hat{\sigma}_{es0}$	Saturation threshold stress at 0 K	801.01 MPa
$\dot{\varepsilon}_{s0}$	Reference strain rate of saturation threshold stress	$1.0x10^{7}$ s^{-1}
a_0	Constant of hardening function	67604.6 MPa
a_1	Constant of hardening function	1816.9 MPa
a_2	Constant of hardening function	202.3 MPa
b_0	Shear modulus at 0 K	28.83 GPa
b_1	Shear modulus constant	4.45 GPa
b_2	Shear modulus constant	248.5 K
T_r	Reference temperature	293.15 K
ρ	Density	2.81 g cm^{-3}
C_p	Heat capacity	896 J/kg K

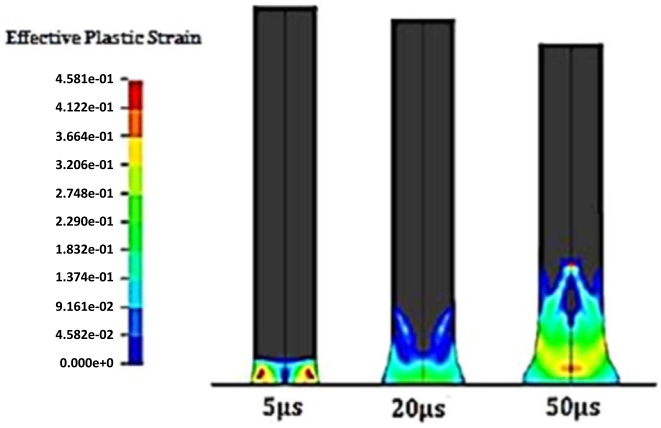

Fig. 20. Deformed profiles (mushroom-shape) of the impact cylinder at various instants.

higher velocity. In this figure, it can be observed that the generated plastic wave has caused a severe deformation in a radial motion moving away from the cylinder's axial axis. Therefore, the highest effective strain shown is developed in the middle of the cylinder footprints. A higher impact velocity again is expected to produce a higher effective plastic strain around the localized deformation area compared to a lower impact velocity. This radial deformation mode that is correctly predicted at the bottom area helps the proposed constitutive model to produce an axial shortening of the cylinders.

The propagation of the elastic compression wave is also observable in the simulation test. Consequently, this deformation behaviour ensured there is no plastic deformation developed at the top of the cylinders as the effective plastic strain continues raise from the bottom to the top of the cylinders and ceases somewhere in the middle of the cylinders. By using the simulation test data, radial strain vs. distance from impact end curves of the new constitutive model against the experimental result are plotted in Fig. 21.

In this figure, the major and minor side profiles of the deformed cylinder are compared in the case of 200 ms^{-1} impact velocity. Generally, it can be seen that the increment in the footprint radius has an inverse relation with the shortening of the cylinder length. These criteria are directly influenced by the value of impact velocity. In addition, Fig. 21 shows a good agreement between the new constitutive model and the experimental results in terms of both final footprint radius and length of the deformed cylinder in the case of 200 ms^{-1}

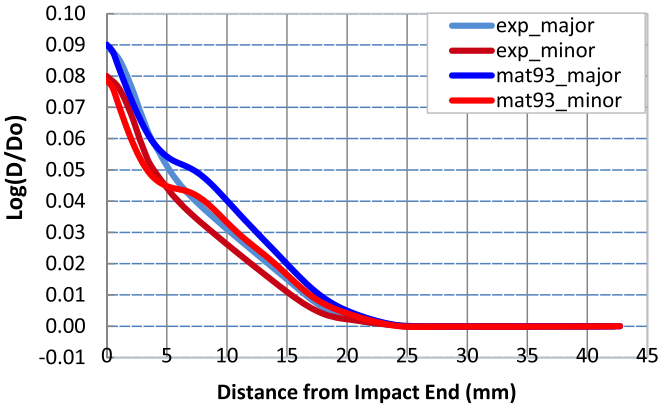

Fig. 21. Major and minor side profile of Taylor cylinder experimental test results against simulation results (plotted as radial strain vs distance).

impact velocity. The only deviation between the simulation and the experimental results is related to the developed mushroom-shape. It can be observed that the new constitutive model has captured a slightly different mushroom-shape with respect to the experimental results.

The analysis on this deviation must be referred back to the previous discussion related to the Taylor Impact test deformation mode. As emphasized, the deformation is developed at the bottom, near to the impact area and raised to the top of the cylinder. This is due to the propagation of the plastic compressive wave which is accompanied by plastic deformation. In the new constitutive model, the plastic deformation or effective plastic strain is controlled by a flow stress formulation which refers to the MTS physically-based model. Therefore, the mushroom-shape disagreement between simulation and experiment of this analysis is potentially affected by the parameters used to characterize the proposed constitutive model. The MTS parameters used in this analysis are previously derived with new procedures in Villi's work [56] Further work is required to justify this hypothesis. However, it is reasonable to suggest that potentially only a few parameters might not be correctly derived since the footprint radius and the final length of the deformed cylinder are satisfactorily captured.

From the analysis performed in this section, it can be observed the proposed formulation of the new constitutive model integrated in the isoclinic configuration and updated in a unique alignment of deviatoric plane within the stress space is capable of producing a good agreement with respect to the Taylor Cylinder Impact test data of orthotropic metals. At this point, it can be concluded that the validation process is completed since the capability of the proposed formulation of the new constitutive model to simulate the deformation behaviour of orthotropic metals at high strain rates within a three-dimensional stress-state has finally been validated.

5. Conclusion

A new hyperelastic-plastic constitutive model for orthotropic metals undergoing finite deformation is discussed in this paper. The objective of this study is to develop a new constitutive model for orthotropic metals that takes into consideration the influence of strain rate and temperature by adopting the new generalized pressure proposed for orthotropic materials.

The proposed constitutive model used a new Mandel stress tensor that is combined with the new stress tensor decomposition of generalized pressure. In addition, the Mechanical Threshold Model (MTS) is adopted as a referential curve to control the yield surface expansion that accounts for isotropic plastic hardening. Furthermore, the formulation is developed in the isoclinic configuration using the multiplicative decomposition of the deformation gradient framework, which further combined with Equation of States (EOSs).

The newly implemented constitutive model is finally validated *by a comparison against a Plate Impact test and Taylor Cylinder Impact test results*. The results are satisfactory with respect to the experimental data after its rate and temperature sensitivities are investigated.

The proposed formulation is the key novelty of this work – and in fact a new finding in this field. The expansion of orthotropic yield surface is performed in a unique alignment of deviatoric plane that is shifted away from the conventional alignment defined uniquely by the elastic properties of orthotropic materials. This achievement is a good indication for more appropriate orthotropic constitutive models in future in order to help towards a better understanding of the complexity of material orthotropy undergoing finite deformation.

Acknowledgement

The author wishes to convey a sincere gratitude to Universiti Tun Hussein Onn Malaysia (UTHM), and Ministry of Higher Education Malaysia for providing the financial means during the preparation to complete this work under Fundamental Research Grant Scheme (FRGS), Vot 1547.

References

[1] C.E. Anderson, P.A. Cox, G.R. Johnson, P.J. Maudlin, A constitutive formulation for anisotropic materials suitable for wave propagation computer program-II, Comput. Mech. 15 (1994) 201–223.
[2] N. Aravas, Finite-strain anisotropic plasticity and the plastic spin, Model. Simul. Mater. Sci. 2 (1994) 483–504.
[3] J.R. Asay, M. Shahinpoor, High-Pressure Shock Compression of Solids, Springer, New York, 1993.
[4] D. Banabic, H.J. Bunge, K. Pohlandt, A.E. Tekkaya, Formability of Metallic Materials, Springer, Heidelberg, 2000.
[5] D. Banabic, T. Kuwabara, T. Balan, D.S. Comsa, D. Julean, Non-quadratic yield criterion for orthotropic sheet metals under plane-stress conditions, J. Mech. Sci. 45 (2003) 797–811.
[6] F. Barlat, J. Lian, Plastic behaviour and stretchability of sheet metals. Part I: a yield function for orthotropic sheets under plane stress conditions, Int. J. Plast. 5 (1989) 51–66.
[7] F. Barlat, D. Lege, J. Brem, A six-component yield function for anisotropic materials, Int. J. Plast. 7 (1991) 693–712.
[8] F. Barlat, H. Aretz, J.W. Yoon, M.E. Karabin, J.C. Brem, R.E. Dick, Linear transformation based anisotropic yield functions, Int. J. Plast. 21 (2005) 1009–1039.
[9] F. Barlat, Y. Maeda, K. Chung, M. Yanagawa, J. Brem, Y. Hayashida, D. Lege, K. Matsui, S. Murtha, S. Hattori, R. Becker, S. Makosey, Yield function development for aluminium alloy sheet, J. Mech. Phys. Solids 45 (1997) 1727.
[10] T. Belytschko, W.K. Liu, B. Moran, Nonlinear Finite Elements for Continua and Structures, John Wiley & Sons Ltd, Chichester, 2000.
[11] J.P. Boehler, On irreducible representations for isotropic scalar functions, ZAMM 57 (1977) 323–327.
[12] C.A. Bronkhorst, E.K. Cerreta, Q. Xue, P.J. Maudlin, T.A. Mason, G.T. Gray III, An experimental and numerical study of the localization behaviour of tantalum and stainless steel, Int. J. Plast. 22 (7) (2006) 1304–1335.
[13] O. Cazacu, F. Barlat, Application of representation theory to describe yielding of anisotropic aluminum alloys, Int. J. Eng. Sci. 41 (2003) 1367–1385.
[14] O. Cazacu, B. Plunkett, F. Barlat, Orthotropic yield criterion for hexagonal closed packed metals, Int. J. Plast. 22 (2006) 1171–1194.
[15] K. Chung, K. Shah, Finite element simulation of sheet forming for planar anisotropic metals, Int. J. Plast. 8 (1992) 453–476.
[16] J.D. Colvin, R.W. Minich, D.H. Kalantar, A model for plasticity kinetics and its role in simulating the dynamic behaviour of Fe at high strain rates, Int. J. Plast. 25 (4) (2009) 603–611.
[17] Y.F. Dafalias, Orientational evolution of plastic orthotropy in sheet metals, J. Mech. Phys. Solids 48 (2000) 2231–2255.
[18] L. Davison, R.A. Graham, Shock compression of solids, Phys. Rep. 55 (1979) 255–379.
[19] D.S. Drumheller, Introduction to Wave Propagation in Nonlinear Fluids and Solids, Cambridge University Press, Cambridge, UK, 1998.
[20] B. Eidel, F. Gruttmann, Elastoplastic orthotropy at finite strains: multiplicative formulation and numerical implementation, Comput. Mater. Sci. 28 (2003) 732–742.
[21] S. Eliezer, A. Ghatak, H. Hora, E. Teller, An Introduction to Equations of State, Theory and Applications, Cambridge University Press, Cambridge, 1986.
[22] H.P. Feigenbaum, Y.F. Dafalias, Directional distortional hardening in metal plasticity within thermodynamics, Int. J. Solids Struct. 44 (2007) 7526–7542.
[23] H.P. Feigenbaum, Y.F. Dafalias, Simple model for directional distortional hardening in metal plasticity within thermodynamics, ASCE J. Eng. Mech. 134 (9) (2008) 730–738.
[24] P.S. Follansbee, U.F. Kocks, A constitutive description of the deformation of copper based on the use of the mechanical threshold stress as internal state variable, Acta Metall. 36 (1988) 81–93.
[25] M.D. Furnish, L.C. Chhabildas, Alumina strength degradation in the elastic regime, in: AIP Conference Proceedings, vol. 429(1), 1988, pp. 501–504.
[26] M. Gotoh, A theory of plastic anisotropy based on a yield function of fourth order (plane stress state)—I/II, Int. J. Mech. Sci. 19 (505–512) (1977) 513–520.
[27] G.T. Gray, N.K. Bourne, J.C.F. Millett, Shock response of tantalum: lateral stress and shear strength through the front, J. Appl. Phys. 94 (10) (2003) 6430–6436.
[28] E. Gruneisen, The state of solid body, NASA R19542 (1959).
[29] R. Hill, A theory of the yielding and plastic flow of anisotropic metals, Proc. R. Soc. (1948) 281–297.
[30] R. Hill, Theoretical plasticity of textured aggregates, Math. Proc. Camb. Philos. Soc. 85 (1979) 179–191.
[31] R. Hill, Constitutive modelling of orthotropic plasticity in sheet metals, J. Mech. Phys. Solids 38 (3) (1990) 405–417.
[32] R. Hill, A user friendly theory of orthotropic plasticity in sheet metals, Int. J. Mech. Sci. 35 (1) (1993) 19–25.
[33] G.A. Holzapfel, Nonlinear Solid Mechanics, A Continuum Approach for Engineering, John Wiley & Sons Ltd, Chichester, 2007.
[34] W.F. Hosford, 1988. Limitations of Non-Quadratic Anisotropic Yield Criteria and Their Use in Analysis of Sheet Forming, In: *Proc. of the 15th IDDRG Congr. A.S.M.*, Dearborn, MI, pp. 163–170.
[35] K. Inal, P.D. Wu, K.W. Neale, Simulation of earing in textured aluminum sheets, Int. J. Plast. 16 (2000) 635–648.
[36] M. Itskov, On the application of the additive decomposition of generalized strain measures in large strain plasticity, Mech. Res. Commun. 31 (2004) 507–517.
[37] M. Itskov, N. Aksel, A constitutive model for orthotropic elasto-plasticity at large strains, Arch. Appl. Mech. 74 (2004) 75–91.
[38] G.I. Kanel, E.B. Zaretsky, A.M. Rajendran, S.V. Razorenov, A.S. Savinykh, V. Paris, Search for conditions of compressive fracture of hard brittle ceramics at impact loading, Int. J. Plast. 25 (4) (2009) 649–670.
[39] A.P. Karafillis, M.C. Boyce, A general anisotropic yield criterion using bounds and a transformation weighting tensor, J. Mech. Phys. Solids 41 (1993) 1859–1886.
[40] A.S. Khan, C.S. Meredith, Thermo-mechanical response of Al 6061 with and without equal channel angular pressing (ECAP), Int. J. Plast. 26 (2) (2010) 189–203.
[41] A.S. Khan, R. Kazmi, B. Farrokh, Multiaxial and non-proportional loading responses, anisotropy and modeling of Ti–6Al–4V titanium alloy over wide ranges of strain rates and temperatures, Int. J. Plast. 23 (6) (2007) 931–950.
[42] A.S. Khan, R. Kazmi, B. Farrokh, M. Zupan, Effect of oxygen content and microstructure on the thermo-mechanical response of three Ti–6Al–4V alloys: experiments and modeling over a wide range of strain-rates and temperatures, Int. J. Plast. 23 (7) (2007) 1105–1125.
[43] A.S. Khan, R. Kazmi, A. Pandey, T. Stoughton, Evolution of subsequent yield surfaces and elastic constants with finite plastic deformation. Part-I: a very low work hardening aluminum alloy (Al6061-T6511), Int. J. Plast. 25 (9) (2009) 1611–1625.
[44] R.W. Logan, W.F. Hosford, Upper-bound anisotropic yield locus calculations assuming (111)-pencil glide, Int. J. Mech. Sci. 22 (1980) 419.
[45] C. Man, On the correlation of elastic and plastic anisotropy in sheet metals, J. Elast. 39 (2) (1995) 165–173.
[46] J. Mandel, Plasticité Classiqueet ViscoplastiéCISM lecture Notes, Springer-Verlag, Wien, 1972.
[47] P.J. Maudlin, J.F. Bingert, J.W. House, S.R. Chen, On the modeling of the Taylor cylinder impact test for orthotropic textured materials: experiments and simulations, Int. J. Plast. 15 (2) (1999) 139–166.
[48] P.J. Maudlin, G.T. Gray III, C.M. Cady, G.C. Kaschner, High-rate material modelling and validation using the Taylor cylinder impact test, Philos. Trans. R. Soc. A: Math. Phys. Eng. Sci. 357 (1756) (1999) 1707–1729.
[49] C.S. Meredith, A.S. Khan, Texture evolution and anisotropy in the thermo-mechanical response of UFG Ti processed via equal channel angular pressing, Int. J. Plast. 30–31 (2012) 202–217.
[50] M.A. Meyers, Dynamic Behaviour of Materials, Wiley, Inc, New York, 1994.
[51] R. Minich, J. Cazamias, M. Kumar, A. Schwartz, Effect of microstructural length scales on spall behaviour of copper, Metall. Mater. Trans. A 35 (9) (2004) 2663–2673.
[52] M.K. Mohd Nor, R. Vignjevic, J. Campbell, Modelling of shockwave propagation in orthotropic materials, Appl. Mech. Mater. 315 (2013) 557–561.
[53] M.K. Mohd Nor, R. Vignjevic, J. Campbell, Plane-stress analysis of the new stress tensor decomposition, Appl. Mech. Mater. 315 (2013) 635–639.
[54] F.J. Mont´ans, K.J. Bathe, Towards a Model for Large Strain Anisotropic Elasto-PlasticityComputational Plasticity, Springer, Berlin, 2007, p. 2007 (13-36.©).
[55] E. Nakamachi, N.N. Tam, H. Morimoto, Multi-scale finite element analyses of sheet metals by using SEM-EBSD measured crystallographic RVE models, Int. J. Plast. 23 (3) (2007) 450–489.
[56] V. Panov, Modelling of Behaviour of Metals at High Strain Rates (Ph.D. dissertation), Cranfield University, Cranfield, 2006.
[57] B. Plunkett, R.A. Lebensohn, O. Cazacu, F. Barlat, Anisotropic yield function of hexagonal materials taking into account texture development and anisotropic hardening, Acta Mater. 54 (2006) 4159–4169.
[58] B. Plunkett, O. Cazacu, R.A. Lebensohn, F. Barlat F, Elastic-viscoplastic anisotropic modeling of textured metals and validation using the Taylor cylinder impact test, Int. J. Plast. 23 (6) (2007) 1001–1021.
[59] S. Reese, I.N. Vladimirov, Anisotropic modelling of metals in forming processes, in: Proceedings of the IUTAM Symposium on Theoretical Computational and Modelling Aspects of Inelastic Media, vol. 11, 2008, pp. 175–184.

[60] Z. Rosenberg, G. Luttwak, Y. Yeshurun, Y. Partom, Spall studies of differently treated 2024A1 specimens, J. Appl. Phys. 54 (5) (1983) 2147–2152.
[61] C. Sansour, I. Karsaj, J. Soric, A formulation of anisotropic continuum elastoplasticity at finite strains. Part I: modelling, Int. J. Plast. 22 (2006) 2346–2365.
[62] C. Sansour, I. Karsaj, J. Soric, On anisotropic flow rules in multiplicative elastoplasticity at finite strains, Comput. Methods Appl. Mech. Eng. 196 (2007) 1294–1309.
[63] C. Sansour, I. Karsaj, J. Soric, On a numerical implementation of a formulation of anisotropic continuum elastoplasticity at finite strains, J. Comput. Phys. 227 (2008) 7643–7663.
[64] J. Schröder, K. Hackl (2014) Plasticity and Beyond: Microstructures, Crystal-Plasticity and Phase Transitions, CISM International Centre for Mechanical Sciences, Springer.
[65] J. Schröder, F. Gruttmann, J. Löblein, A simple orthotropic finite elasto–plasticity model based on generalized stress–strain measures, Comput. Mech. 30 (2002) 48–64.
[66] S. Sinha, S. Ghosh, Modeling cyclic ratcheting based fatigue life of HSLA steels using crystal plasticity FEM simulations and experiments, Int. J. Fatigue 28 (12) (2006) 1690–1704.
[67] M. Sitko, B. Skoczeń, A. Wróblewski, FCC-BCC phase transformation in rectangular beams subjected to plastic straining at cryogenic temperatures, Int. J. Mech. Sci. 52 (7) (2010) 993–1007.
[68] R.E. Smallman, Modern Physical Metallurgy, fourth ed., Butterworths, London, 1985.
[69] D.J. Steinberg, Equation of State and Strength Properties of Selected Materials, Report No. UCRL-MA-106439, Lawrence Livermore National Laboratory, Livermore, CA, 1991.
[70] P. Tugcu, K.W. Neale, On the implementation of anisotropic yield functions into finite strain problems of sheet metal forming, Int. J. Plast. 16 (1999) 701–720.
[71] R. Vignjevic, N. Djordjevic, V. Panov, Modelling of dynamic behaviour of orthotropic netals including damage and failure, Int. J. Plast. 38 (2012) 47–85.
[72] R. Vignjevic, N.K. Bourne, J.C.F. Millett, T. De Vuyst, Effects of orientation on the strength of the aluminum alloy 7010-T6 during shock loading: experiment and simulation, J. Appl. Phys. 92 (8) (2002) 4342–4348.
[73] R. Vignjevic, J. Campbell, N.K. Bourne, N. Djordjevic, Modelling Shock Waves in Orthotropic Elastic Materials – Conference on Shock Compression of Condensed Matter, Hawaii.
[74] I.N. Vladimirov, M.P. Pietryga, S. Reese, On the modelling of non-linear kinematic hardening at finite strains with application to springback – comparison of time integration algorithms, Int. J. Numer. Methods Eng. 75 (1) (2008) 1–28.
[75] J. Wackerle, Shock-wave compression of quartz, J. Appl. Phys. 33 (1962) 922–937.
[76] M.J. Worswick, M.J. Finn, The numerical simulation of stretch flange forming, Int. J. Plast. 16 (2000) 701–720.
[77] E.B. Zaretsky, G.I. Kanel, Plastic flow in shock-loaded silver at strain rates from 10[sup 4]s[sup-1] to 10[sup 7]s[sup-1] and temperatures from 296 K to 1233 K, J. Appl. Phys. 110 (7) (2011) 073502.
[78] Y.B. Zel'dovich, Y.P. Raizer, In: Physics of Shock Waves and High-temperature Hydrodynamic Phenomena, vols. 1–2, Academic Press, New York, 1966.
[79] Q.S. Zheng, Theory of representations for tensor functions – a unified invariant approach to constitutive equations, Appl. Mech. Rev. 47 (11) (1994) 545.